WIND
ENERGY
SCIENCE

eawe
european academy of wind energy

Open Access

Improving wind and power predictions via four-dimensional data assimilation in the WRF model: case study of storms in February 2022 at Belgian offshore wind farms

Tsvetelina Ivanova[1,2], **Sara Porchetta**[3,4], **Sophia Buckingham**[5], **Gertjan Glabeke**[1,6], **Jeroen van Beeck**[1], and **Wim Munters**[1]

[1]Environmental and Applied Fluid Dynamics Department, von Karman Institute for Fluid Dynamics, Chau. de Waterloo 72, 1640 Rhode-Saint-Genèse, Belgium
[2]Department of Engineering Technology, Vrije Universiteit Brussel, Pleinlaan 2, 1050 Brussels, Belgium
[3]Civil and Environmental Engineering, Massachusetts Institute of Technology, 77 Massachusetts Avenue, 1–290, Cambridge, MA 02139, United States of America
[4]Department of Geoscience and Remote Sensing, Faculty of Civil Engineering and Geosciences, Delft University of Technology, Stevinweg 1, 2628 CN Delft, the Netherlands
[5]Research & Innovation, ENGIE Laborelec, Rodestraat 125, 1630 Linkebeek, Belgium
[6]Department of Civil Engineering, Hydraulics Laboratory, Ghent University, Sint-Pietersnieuwstraat 41, 9000 Gent, Belgium

Correspondence: Tsvetelina Ivanova (tsvetelina.ivanova@vki.ac.be)

Abstract. Accurate modeling of wind conditions is vital for the efficient operation and management of wind farms. This study investigates the enhancement of weather simulations by assimilating local offshore light detection and ranging (lidar) and/or supervisory control and data acquisition (SCADA) data into a numerical weather prediction model while considering the presence of neighboring wind farms through wind farm parameterization. We focus on improving model output during storms impacting the Belgian–Dutch wind farm cluster located in the Southern Bight of the North Sea via the four-dimensional data assimilation (nudging) technique in the Weather Research and Forecasting (WRF) model. Our findings indicate that assimilating wind observations significantly reduces the relative root-mean-square error for wind speed at a wind farm located 47 km downwind from the offshore lidar platform. This leads to more accurate power production outputs. Specifically, at wind turbines experiencing wake effects, the wind speed error decreased from 10.5 % to 5.2 %, and the wind direction error was reduced by a factor of 2.4. A proposed artificial configuration, leveraging the upwind lidar measurements, showcases the potential for improving hour-ahead wind and power predictions. Moreover, we perform a thorough study to investigate the sensitivity to nudging parameters during versatile atmospheric conditions, which helps to identify the best assimilation practices for this offshore setting. These insights are expected to refine wind resource mapping and reanalysis of weather events, as well as motivate more measurement campaigns offshore.

1 Introduction

In recent years, wind energy has emerged as a crucial and rapidly growing renewable energy source. Accurate numerical simulation of wind speed, wind direction, and power production has become essential for efficient planning, design, and operation of wind farms. The use of numerical weather prediction (NWP) models, such as the open-source Weather Research and Forecasting (WRF) model (Skamarock et al., 2019), developed at the National Center for Atmospheric Research (NCAR), plays a vital role in obtaining these accurate model outputs.

For weather simulations at offshore wind farm zones, NWP models do not necessarily have sufficiently accurate initial conditions due to the sparsity of offshore observations. This lack of data leads to broader issues, where NWP models can display large bias errors due to the overall lack of long-term offshore measurement data (Archer et al., 2014). Furthermore, extreme events in which wind turbines are still operating can have a profound impact on wind farm operations. Such events involving high wind speeds can often lead to implications for power generation and grid stability. The impact at near-ground levels can be damaging for human activity and can cause grid instabilities and potential wind turbine cut-outs. This further increases the need for accurate weather simulations. Numerous works are dedicated to studying and understanding extreme events, such as Larsén et al. (2019), Pryor and Barthelmie (2021), Vemuri et al. (2022), and Sethunadh et al. (2023). Given that extreme events are often influenced by the larger-scale dynamics of the atmosphere, NWP models are commonly employed to analyze and predict them. However, accurately capturing extreme events that significantly impact wind energy remains a challenge.

Improving wind and power simulations extends beyond model settings and can be enhanced by incorporating additional physics. One such path to consider is the impact of wind farms on the atmosphere. In NWP models, wind farms can be represented by a wind farm parameterization (WFP). Over the years, different WFPs have been proposed. By employing WFP, the influence of wind farms on the surrounding atmospheric conditions is accounted for, and, consequently, an insight into approximated inter-farm dynamics is possible. A study by Lee and Lundquist (2017) quantifies wind and power prediction improvements that are achieved by incorporating WFP. A systematic literature review by Fischereit et al. (2022a) compares 10 existing WFPs. Furthermore, Fischereit et al. (2022b) highlight that the WFP of Fitch et al. (2012) is a suitable state-of-the-art choice for modeling the presence of wind farms in WRF and is selected in the present work. This WFP models the wind farm as a momentum sink and a turbulent kinetic energy (TKE) source. Other WFP applications include wind–wave coupling studies, such as Porchetta et al. (2021). Accurately capturing atmospheric conditions is crucial for modeling wind farm wakes. However, when representing wind farm wakes in mesoscale models using WFP, uncertainties arise (Eriksson et al., 2017; Peña et al., 2022; Ali et al., 2023). WFP has limitations, including the need for TKE correction, as well as its sensitivity to atmospheric stability. Additionally, WFPs restrict options for planetary boundary layer schemes in NWP models, which in turn affects the fidelity of boundary layer representation.

Along with model setting and including more physics within WRF, improvements in wind and power model output can also be achieved by employing data assimilation (DA) techniques. Data assimilation is the process of integrating observed data into a numerical model (Skamarock et al., 2019). We distinguish between two groups of such techniques: variational DA (Barker et al., 2012) and four-dimensional data assimilation (FDDA or nudging; Liu et al., 2008). Variational DA is concerned with finding the optimal initial state of the atmosphere (in the case of three-dimensional variational data assimilation (3DVar), Barker et al., 2004) and, furthermore, the optimal model trajectory based on this optimal initial state (in the case of four-dimensional variational data assimilation (4DVar), Huang et al., 2009; Zhang et al., 2013, 2014). Both 3D and 4D variational DA techniques rely on minimizing the difference between model forecasts and observations by optimizing a cost function. One work that exploits the benefits of variational data assimilation is by Sun et al. (2022), in which wind speed forecasts are improved when assimilating observations from the nacelle of turbines. In contrast, FDDA (nudging) operates differently from variational data assimilation: FDDA directly influences the state variables over time in order to match observed data (Reen, 2016; Reen and Stauffer, 2010), and it is the selected method in this work. In FDDA, the approach is to introduce tendency terms in the model equations to adjust the prognostic variables, such as temperature, humidity, and wind components, towards observed values. This approach acts as a controller rather than a cost function optimizer. This makes FDDA much more computationally efficient than variational methods, and this is highly relevant in an operational context (Cheng et al., 2017). A drawback of this method is that only prognostic model variables can be assimilated. Besides observational FDDA, it is also possible to perform grid nudging and spectral nudging in WRF: these are out of the scope of this work. Several studies have explored the leverage of data assimilation techniques in mesoscale models for wind energy applications. For example, Kosovic et al. (2020) use real-time FDDA (RTFDDA) for local data, integrated with a machine learning approach for power estimation. Nudging techniques are also applied in the onshore study of Cheng et al. (2017) that highlights the effectiveness of RTFDDA (within a customized version of WRF) in improving wind energy predictions 0–3 h ahead for normal weather conditions, using only wind speed observations from wind turbine anemometers. Furthermore, in their study, Mylonas et al. (2018) perform FDDA of observations from the offshore meteorologi-

cal mast FINO3 in the North Sea for wind resource assessment and reanalysis.

Our research presents a novel approach to improving wind and power model output by integrating the advantages of a physics-based WFP and FDDA in WRF, particularly during extreme offshore conditions. We focus on utilizing observational FDDA of horizontal wind components gathered from a light detection and ranging (lidar) vertical profiler. This approach is unique in its offshore application of FDDA in WRF due to the strategic placement of the lidar upstream (with respect to the most common southwesterly winds in the Southern Bight of the North Sea). This geographical advantage allows for advanced information on incoming wind conditions to be provided approximately 1 h ahead, which is the advective time required. Our goal is to improve the accuracy of wind and power model output offshore by assimilating this data during significant events, such as the storms Eunice and Franklin in February 2022 over the Belgian North Sea. These events had a substantial impact on wind power production (reported, for example, in Belgian Offshore Platform News, 2022), making them crucial case studies for our research. Furthermore, to gain insight into optimal FDDA settings for this offshore configuration, we experiment with sensitivity to different observational nudging parameters, such as nudging strength and the horizontal radius of the influence of the assimilated observations. We evaluate the performance of the simulations by comparing the results to lidar and supervisory control and data acquisition (SCADA) datasets, using classic metrics from the state-of-the-art handbook on wind forecasting by Yang et al. (2021). These metrics are mean absolute error (MAE), root-mean-square error (RMSE), and bias with respect to observations.

The paper is structured as follows. Section 2 describes the methodology and the configuration of the numerical setup of the WRF model, including the FDDA algorithm, the available offshore observations, and selected case studies for simulations in this work. Section 3 expresses the results and discussion for different simulation scenarios. Finally, Sect. 4 outlines the conclusions of this paper.

2 Methodology and numerical setup

The NWP model employed in this work is the Advanced Research WRF (ARW) model (Skamarock and Klemp, 2008; Skamarock et al., 2019), version 4.5.1, which is a state-of-the-art mesoscale NWP system available in the public domain. It solves the fully compressible non-hydrostatic Euler equations, and it has a rich set of physics parameterizations.

2.1 The WRF model configuration

Our study is focused on the Belgian–Dutch wind farm cluster. The setup consists of five nested domains, three of which are identical and innermost. The domains have the following names and grid cells: D01 – 150×150; D02 – 190×190; and D03, D04, and D05 – 220×190 grid cells, centered at latitude $51.42°$ N and longitude $2.74°$ E, with one-way nesting. The Lambert conformal projection is selected. The three identical innermost domains, D03, D04, and D05, are of interest, with a size of 680 km by 596 km. The horizontal grid spacing is 18 km for the outer domain, 6 km for the intermediate domain, and 2 km for the three innermost domains. The latter follows the guidelines of Fischereit et al. (2022a) to use horizontal grid spacing of at least 3 to 5 times the wind turbine rotor diameter for the domains with active WFP (in this case, D04 and D05). The model configurations in the three innermost domains (with 2 km grid spacing) differ in the following way: D03 is for simulations without WFP, D04 is for active WFP, and D05 is for active WFP while performing FDDA. The domains are shown in Fig. 1, along with key measurement locations of three lidars: at the Westhinder (WHi) platform (Glabeke et al., 2023), the Lichteiland Goeree (LEG) platform, and the Europlatform (EPL) (TNO Wind Energy Research Group, 2023).

The setup in this work is based on Hahmann et al. (2020), Dörenkämper et al. (2020), and Larsén and Fischereit (2021). Relevant details on the parameterizations used in the setup can be found in Table 1. The cumulus scheme is used only on the outermost domain. Our study involves usage of the WFP of Fitch et al. (2012), which further requires the introduction of sufficient vertical model levels. This allows for a representative description of the wind profile across the rotor, which is done by relying on recommendations from Lee and Lundquist (2017). The vertical levels are stretched, which ensures more levels close to the surface. The total number of levels is 80 (Lee and Lundquist, 2017). The lowest level is at 6 m, with sufficient points across the wind turbine rotor for a typical offshore wind turbine (WT) in the Belgian–Dutch cluster. More specifically, for the smallest wind turbine within the Belgian side of the Belgian–Dutch cluster, there are 8 vertical levels that span across the rotor, whereas for the largest wind turbine of this cluster, there are 15 levels. The model pressure top is at 1000 Pa.

To consider the impact of wind farms, we incorporate not only the Belgian–Dutch wind farm cluster, but also the fully commissioned offshore wind farms in the Southern Bight of the North Sea via the WFP of Fitch et al. (2012) within the WRF model. This group of wind farms consists of 1409 wind turbines (out of 5779 in total in Europe and the UK; Hoeser et al., 2022) within 27 different wind farms that are represented in the setup, in proximity to the Belgian–Dutch cluster. The locations of these wind farms are extracted from Hoeser et al. (2022) and the publicly available dataset of Hoeser and Kuenzer (2022). The details of the different wind farms are summarized in Table A1. Besides wind turbine locations, the WFP requires the power and thrust curves for each wind turbine in order to simulate its effects on the atmosphere. These were obtained from a mix of both open (https://www.thewindpower.net/, last access: 21 January 2025; and WindPRO (EMD-International)) and confi-
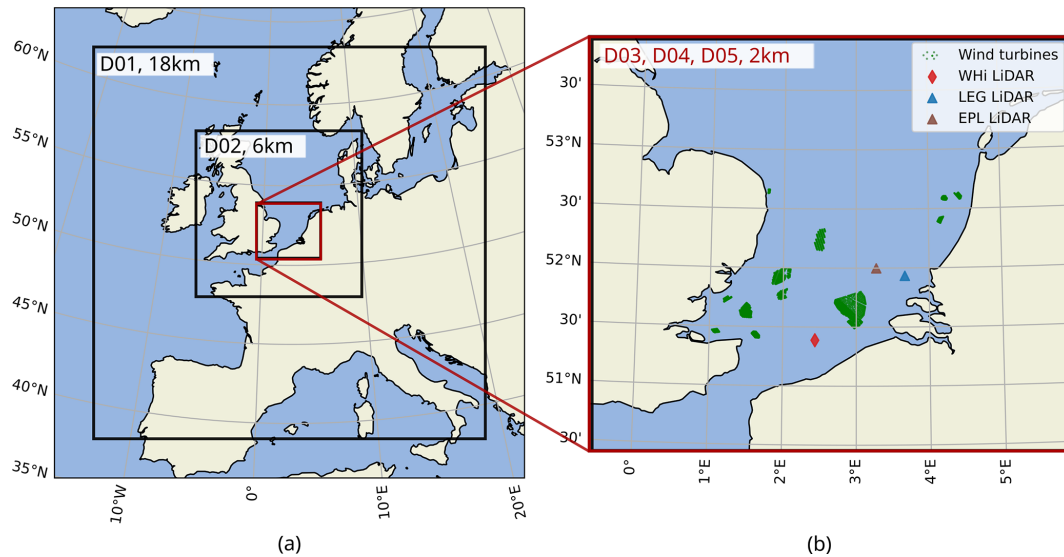
Figure 1. Nested domains in WRF **(a)**. The domains of interest **(b)** are the three identical ones, D03, D04, and D05, with a grid spacing of 2 km. Key measurement locations are indicated (i.e., WHi, LEG, and EPL lidars). The 1409 wind turbines that are currently included in the WRF setup are also visualized in **(b)**.

Table 1. Parameterization options and configuration in the present WRF setup.

Parameterization	Scheme (with option in namelist)	Reference
PBL scheme	MYNN level-2.5 TKE (option 5)	Nakanishi and Niino (2006)
Cumulus	Kain–Fritsch (option 1)	Kain (2004)
Microphysics scheme	Thompson et al. (option 8)	Thompson et al. (2008)
Radiation	RRTMG (option 4)	Iacono et al. (2008)
Land surface model	NOAH LSM (option 2)	Ek et al. (2003)
Wind farm parameterization	when active: Fitch (option 1)	Fitch et al. (2012)
TKE correction coefficient α	0.25 (default value)	Archer et al. (2020)

dential sources. The performed WFP simulations take into account the TKE advection with a correction factor α of 0.25, following Archer et al. (2020). This coefficient α is denoted in Table 1.

For time integration, a third-order Runge–Kutta scheme is used, and for advection, second- to sixth-order spatial discretization schemes are used. For the model integration, adaptive time stepping is used, with a target Courant–Friedrichs–Lewy number of 0.6. For initial and boundary conditions, the Global Forecast System (GFS) 3-hourly data from NCEP's historical archive are used, with forecast grids on a 0.25 by 0.25 global latitude–longitude grid (National Centers for Environmental Prediction et al., 2015). All simulated periods include a 12 h spin-up time. These periods of interest are detailed in Sect. 2.3 and include extreme events in February 2022 (storms Eunice and Franklin).

Our study investigates the sensitivity of results to nudging parameters. Varying such parameters helps to gain insight into the most suitable assimilation strategies for this offshore configuration. For a selected day (17 February 2022), a num-

ber of simulations are performed by varying the horizontal radius of influence R_{xy}, as well as the nudging strength G_q. In these numerical experiments, either lidar or SCADA data are assimilated. The FDDA algorithm is detailed in Sect. 2.2. The full sensitivity experiment is described in Sect. 2.5.

2.2   The FDDA (nudging) algorithm

The WRF model has an implemented algorithm to assimilate prognostic model variables such as the horizontal components of wind speed via the FDDA technique, as described in Skamarock et al. (2019), Reen and Stauffer (2010), and Reen (2016). With this algorithm, the numerical solution is nudged towards observations by introducing tendency terms in the model equations as

$$\frac{\partial q\mu}{\partial t}(x, y, z, t) = F_q(x, y, z, t)$$

$$+ \mu G_q \frac{\sum\limits_{i=1}^{N} W_q^2(i, x, y, z, t)(q_o(i) - q_m(x_i, y_i, z_i, t))}{\sum\limits_{i=1}^{N} W_q(i, x, y, z, t)}, \quad (1)$$

where q is the quantity being nudged (in this work, horizontal wind components that are projected from wind speed and wind direction observations, as in Cheng et al., 2017), μ is the dry hydrostatic pressure, F_q is the physical tendency (or model forcing) term of q, G_q is the nudging strength, N is the total number of observations, W_q is the weighing function in space and time, q_o is the observed value of the quantity of interest, and $q(x_i, y_i, z_i, t)$ is its model value. The working principle is of a proportional controller: with the approaching of the model value to its observed value, the nudging tendency term decreases.

The weighing function W_q can be expressed as the product of horizontal (w_{xy}), vertical (w_σ), and temporal (w_t) contributions (Xu et al., 2002). The contribution w_{xy} is a function of the horizontal radius of influence R_{xy}, w_σ is the vertical weighing function, and w_t is a function of the assimilation time window τ over which an observation is used in the nudging algorithm. The horizontal weighing function is a Cressman-type function given by

$$w_{xy} = \frac{R_{xy}^2 - D^2}{R_{xy}^2 + D^2}, \ 0 \leq D \leq R_{xy}, \quad (2)$$

$$w_{xy} = 0, \ D > R_{xy}, \quad (3)$$

where R_{xy} is the radius of influence, and D is the distance from the observation location to the grid point. The vertical and the temporal weighing functions are also distance-weighted. Further details on observational nudging can be found in Grell et al. (1994) and Xu et al. (2002).

In this work, we perform a study investigating the sensitivity to the horizontal radius of influence R_{xy} and the nudging strength G_q. This sensitivity study is described in Sect. 2.5 with all tested nudging parameter values.

2.3 Available offshore observations

In this section, we detail all offshore observations that are used in this work, both for assimilation in WRF and for simulation performance evaluation. The locations of all offshore observations are indicated in Fig. 2a. These datasets are collected at five different locations by three lidar profilers (at the Westhinder platform (WHi), at the Lichteiland Goeree (LEG) platform, and at the Europlatform (EPL)) and by two groups of wind turbines (SCADA from nacelle anemometers at front and waked WTs).

2.3.1 Lidar profiler at the Westhinder platform (WHi)

The observations used for assimilation are collected by a vertical lidar profiler at the Westhinder survey platform (with coordinates 51°23'18.74'' N, 02°26'16.18'' E). The vertical profiling lidar (ZX 300M) is shown in Fig. 2b. It has been installed at the Westhinder platform since August 2021 and has been collecting wind speed and wind direction information since then (Glabeke et al., 2023). In this study, we utilize WHi lidar data that are available from 4 August 2021 to 18 July 2022 and from 26 January to 6 February 2023. This lidar measures at 11 different heights (34.5, 44.5, 62.5, 79.5, 104.5, 124.5, 149.5, 174.5, 224.5, 274.5, and 324.5 mTAW), as shown in Fig. 2c. The measurement heights are in meters above the Tweede Algemene Waterpassing (mTAW), which means that the average sea level at low tide in Ostend (Belgium) is used as the zero level. This value for Ostend is ± 2.3 m (positive and negative deviations) with respect to the mean sea level. The lidar retrieves wind vector data at a frequency of 1 Hz per height. A full measurement of the vertical profile typically takes 17 s due to the extra time for beam focus adjustment and for additional weather condition measurements used in quality control. Thus, for a 10 min interval, the maximum number of validated wind speed and wind direction measurements is 35. The validation is based on a wind-industry filtering, performed by the lidar software (user manual; ZephIR, 2018), as meteorological conditions can result in non-validated wind data (for example, due to low cloud ceiling, fog, or precipitation). The filtering criteria are selected based on a Det Norske Veritas (DNV) classification.

The location in which the WHi lidar observations are collected is especially favorable, since the measurements are of free-stream wind, given the predominant southwesterly winds (shown in the year-long wind rose in Fig. 2d). This allows information to propagate towards the farm of interest when performing FDDA of these local observations. The typical advection timescale of this propagation is approximately 1 h. Therefore, the assimilation of such upwind data can help improve hour-ahead predictions. This approach is discussed in Sect. 2.5, and the results are discussed in Sect. 3.1.

2.3.2 SCADA from nacelle anemometers at front and waked WTs

The nacelle anemometers gather in situ data on horizontal wind speed and wind direction at the wind farms. Additionally, the SCADA system records power production data. For the purpose of our simulations, we have specifically selected two locations within the Belgian–Dutch cluster (which comprises 572 wind turbines), as depicted in Fig. 2. The first location, referred to as "front WTs", includes a subset of five wind turbines. These turbines are strategically positioned in the front row, aligning with the most common wind direction from the southwest. This alignment is consistent both
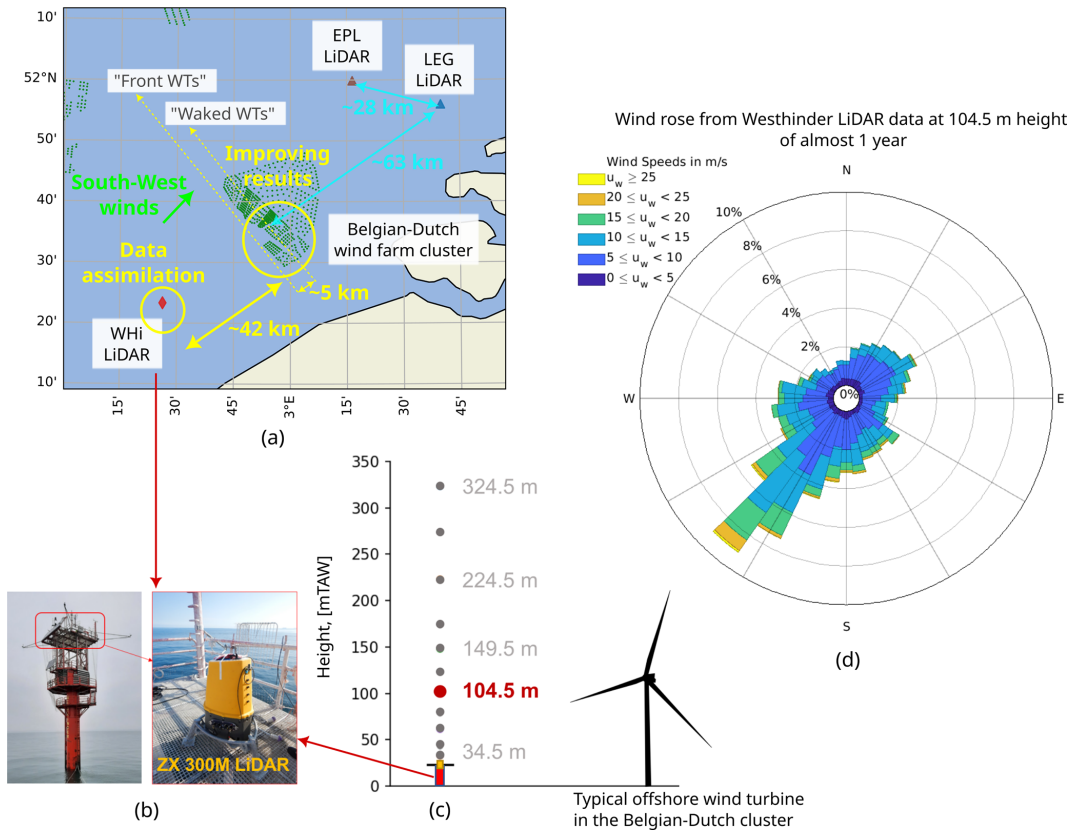
Figure 2. Locations of interest **(a)** within the innermost domains: the (typically) upstream WHi lidar, the front WTs and waked WTs from the Belgian–Dutch cluster, and the LEG and EPL lidars. The WHi lidar is shown on its platform in **(b)**, and its illustration with respect to a typical wind turbine is shown in **(c)**. Finally, a wind rose **(d)** obtained from the lidar dataset of Glabeke et al. (2023) at 104.5 mTAW for a period of almost 1 year (4 August 2021 to 18 July 2022).

for the period under investigation and for the overall prevailing wind direction in the Belgian North Sea, as shown from the wind rose in Fig. 2d. The second location, "waked WTs", consists of another subset of five wind turbines. These turbines are situated in the wake, on an arbitrary back row, of a selected Belgian wind farm (when the wind direction is from the southwest). The selection of these two distinct locations allows us to observe the effect of the wind farm parameterization across a few kilometers. It also enables the assessment of the area of impact of the data assimilation upwind.

The reason for selecting exactly five turbines per location (front WTs and waked WTs) is the computational domain of our simulations. Each subset of turbines is contained within a specific computational cell with a grid spacing of 2 km. Therefore, for both locations, we consider the average values from the SCADA of the corresponding five turbines, providing us with a representative sample for each computational cell. However, due to a non-disclosure agreement with the wind farm operator, we are unable to list the exact coordinates of these turbines.

2.3.3 Lidar at the Lichteiland Goeree (LEG) platform

To further evaluate our numerical results, we compare them additionally to a lidar profiler on the Lichteiland Goeree (LEG) platform (coordinates 51°55′30″ N, 3°40′12″ E) provided by the TNO Wind Energy Research Group (2023) (https://www.tno.nl/, last access: 21 January 2025, https://nimbus.windopzee.net/, last access: 21 January 2025). The LEG platform collects meteorological observations and is positioned approximately 110 km away from the Westhinder platform and approximately 63 km away from the waked WT location, as shown in Fig. 2a. Wind speed observations are obtained via a Leosphere WindCube lidar v2.1, which can measure up to approximately 240 m above sea level (a.s.l.) (eight different heights at 62, 90, 115, 140, 165, 190, 215, and 240 m a.s.l.) simultaneously with a wind vector data rate of 1 Hz.

2.3.4 Lidar at the Europlatform (EPL)

We perform comparisons of simulations with one more lidar ZX 300M wind profiler dataset that is also collected at the Europlatform (EPL) by the TNO Wind Energy Research

Group (2023). The measurement heights of the EPL lidar are 63, 91, 116, 141, 166, 191, 216, 241, 266, and 291 m. This platform is located in proximity to the LEG platform, as indicated in Fig. 2a. The approximate distance between EPL and waked WTs is 56 km.

2.3.5 Performance metrics

The WHi lidar and SCADA datasets (at front and waked WT locations) are utilized for assimilation (nudging) in WRF in distinctive numerical experiments (described in Sect. 2.5), as well as for model output evaluation. Before assimilation in WRF, all wind speed and wind direction observations are projected onto the axes aligned with model U and V velocity variables (Cheng et al., 2017). The results obtained from simulations are compared to the five locations in total, shown in Fig. 2: three lidars (WHi, LEG, and EPL) and two locations (front and waked WTs) with wind turbine data (local wind speed, wind direction, and power) from a SCADA database.

To evaluate the performance of simulations, we utilize established metrics, outlined in Yang et al. (2021). These metrics include mean absolute error (MAE) (Lydia et al., 2014), root-mean-square error (RMSE) (Zhao et al., 2011), and bias (Wang et al., 2019). Each of these metrics provides a different perspective on the accuracy of our simulations compared to offshore observations. Let us denote the ith (normalized) model output variable as p_m^i, the ith (normalized) observed variable as p_o^i, and the length of the dataset as N. The MAE is a widely used metric for evaluating wind model output, as it reflects the overall error level. It is calculated as the average absolute difference between the model output and the observed data:

$$\text{MAE} = \frac{1}{N} \sum_{i=1}^{N} |p_m^i - p_o^i|. \tag{4}$$

The RMSE is another important metric, particularly due to its sensitivity to outliers in NWP model output. It is computed as the square root of the average squared differences between the model output and the observed data:

$$\text{RMSE} = \sqrt{\frac{1}{N} \sum_{i=1}^{N} \left(p_m^i - p_o^i\right)^2}. \tag{5}$$

Lastly, the bias indicates the average deviation of the model output from the actual observed values:

$$\text{Bias} = \frac{1}{N} \sum_{i=1}^{N} \left(p_m^i - p_o^i\right). \tag{6}$$

These metrics allow for a comprehensive analysis and evaluation of model performance across different simulation scenarios.

2.4 Case studies of different weather conditions

The case studies of interest are described in Table 2. For easier reference throughout the text, these cases are labeled as time frames F1 to F4. All four cases have a suitable southwest wind direction that allows for the advection of the assimilated lidar data towards the Belgian–Dutch cluster (Fig. 2a). Each case study has a targeted goal. F1 enhances model accuracy using FDDA. F2 involves a comprehensive analysis of sensitivity to nudging parameters, which is one of the main goals of this work. F3 displays a negative wind speed bias when WFP is inactive, a condition that deteriorates with the activation of WFP due to further momentum extraction from an already underpredicting baseline. Conversely, F4 displays a positive wind speed bias when WFP is inactive, which is reduced once WFP is activated. Thus, for F1, F3, and F4, incorporating FDDA is explored to enhance model output. All times indicated in the figures are in the UTC time zone.

Time frame F1 includes two storms (Eunice and Franklin) in February 2022. The goal within F1 is to use FDDA (of upwind lidar) to help improve model performance. For F1 at the WHi lidar location, according to the observations in Fig. 3 at 104.5 mTAW height, the storms have the following characteristics:

- Storm Eunice occurred from the early morning of 18 February to the early morning of 19 February. It reached a peak velocity of 37.13 m s^{-1} at 14:00 UTC on 18 February 2022, with the wind direction varying between 225 and 275°.

- Storm Franklin spanned the afternoon of 20 February to noon on 21 February. The peak velocity recorded up to 30.46 m s^{-1} at 19:30 UTC on 20 February 2022. Notably, both the wind speed and the direction underwent significant changes, especially from 20:00 to 20:30 UTC on 20 February 2022.

The selection of the F1 period is strategic, given its versatile atmospheric conditions. This period includes instances with wind speeds around the cut-out value, as well as times featuring rapid changes in wind direction. Four-dimensional data assimilation (nudging) is favorable whenever the wind direction is predominantly from the southwest, as this allows for the Westhinder lidar to be upwind from the Belgian–Dutch cluster. This is indeed most often the case in the Southern Bight of the North Sea, as shown in the wind rose in Fig. 2d. The average wind direction for F1 is west-southwest. Note that gaps in the time series in Fig. 3 are due to data filtering performed by the lidar software based on meteorological conditions.

Time frame F2 is a selected day from F1 (17 February 2022), in which we focus on a sensitivity study of the nudging strength and radius of influence to identify optimal FDDA practices. This procedure is detailed in Sect. 2.5. The

Table 2. Time frames of interest in this study along with their corresponding goals.

Label	(Duration) time frame dates	Goal under specific conditions
F1	(4 d) 17–21 February 2022	Improve model performance via FDDA of local upwind lidar data at near hub height
F2	(1 d) 17–18 February 2022	Conduct sensitivity study of nudging strength and horizontal radius of influence to identify optimal FDDA practices
F3	(2 d) 20–22 October 2021	Improve model performance via FDDA for a negative wind speed bias (when WFP is inactive)
F4	(4 d) 30 January–3 February 2023	Improve model performance via FDDA for a positive wind speed bias (when WFP is inactive), including notable wind speed fluctuations
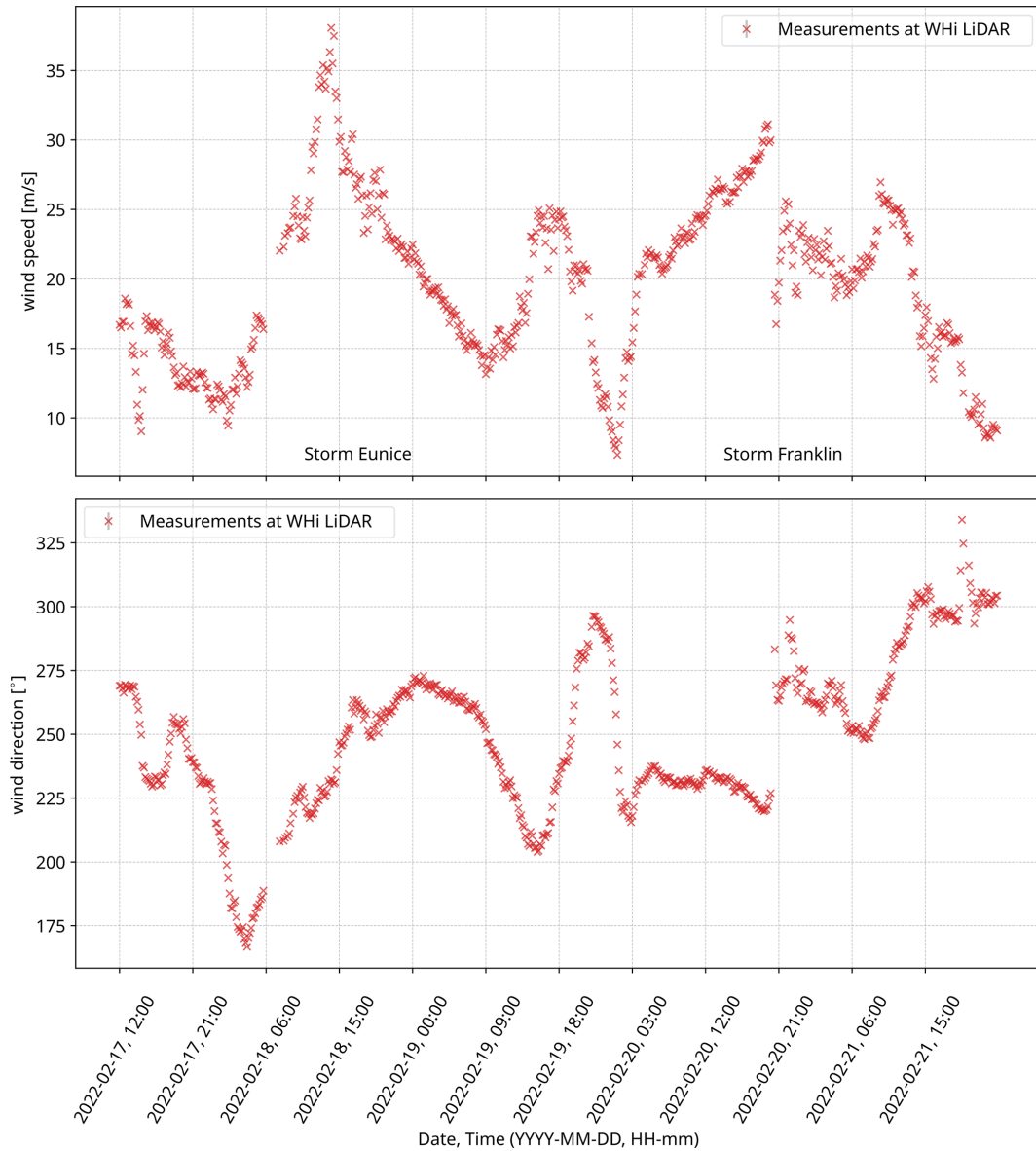
Figure 3. Time frame F1 – lidar observations at 104.5 mTAW height from the Westhinder (WHi) dataset of Glabeke et al. (2023). UTC time zone.

goal in F2 is to understand how different parameters of the FDDA algorithm impact model performance and accuracy and to identify best FDDA practices for the offshore setting.

Time frame F3 spans 2 d, from 20 to 22 October 2021. During this period, we aim to demonstrate the capabilities of a selected FDDA setting (based on the analysis outlined in Sect. 2.5) for a case with a negative bias, specifically when WFP is inactive. This negative bias is even more pronounced when WFP is active (due to the momentum extracted from the flow), making F3 a useful case to test the performance of a selected FDDA setting. Finally, time frame F4 spans 4 d, from 30 January to 3 February 2023. The goal during this period is to demonstrate the capabilities of the selected FDDA setting for a case with a positive bias, again when WFP is inactive. Additionally, this period also involves significant changes in wind speed data. This is identified using a straightforward SCADA data filtering approach, in which a time period is of interest if the difference of two consecutive wind speed data points (5 min apart) is larger than the corresponding standard deviation of $3.93 \, \mathrm{m \, s^{-1}}$. This allows us to test the robustness of the selected FDDA setting under rapidly changing wind conditions.

In each of the time frames (F1, F2, F3, F4), we consistently perform two baseline simulations. The first simulation, referred to as "WFP_off" in subsequent figures, does not account for the presence of wind farms within the computational domain. The second simulation, labeled "WFP", incorporates the effects of these wind farms via the Fitch WFP. Within time frame F2, we perform an extensive set of 20 numerical experiments to assess the sensitivity of results to varying nudging parameters. The details of this study are elaborated on in Sect. 2.5. This helps to identify a preferred (optimal) nudging setting. This setting is then applied to the other case studies, F1, F3, and F4 (labeled "WFP FDDA"). For time frame F1, we conduct a comparative analysis of four distinct numerical experiments (two baseline simulations and two FDDA configurations). In the case of F3 and F4, we carry out three simulations (two baseline and one with FDDA). Finally, to highlight the benefit of offshore measurement campaigns, nudging is applied specifically at near hub height (104.5 m) rather than across the entire lidar profile. This approach underscores the value of such offshore campaigns: even if data collection is spatially limited by weather conditions or technical issues, the data can still provide meaningful input for improving model accuracy.

2.5 Insight into optimal FDDA practices: numerical experiments in F2

In this section, we describe the sensitivity study conducted during time frame F2, from 17 to 18 February 2022. The primary objective of this study is to gain insight into the optimal practices for FDDA, particularly focusing on varying the nudging strength and radius of influence. The specific values

of the nudging parameters used in this study are detailed in Table 3.

Within F2, we perform a sensitivity study examining the impact of the radius of influence and the nudging strength in FDDA. The assimilation of upwind lidar data is performed for 15 numerical experiments (including one configuration where nudging occurs at consecutive intervals) in which we vary the radius of influence R_{xy} and the nudging strength G_q. The assimilation of SCADA is performed for three cases (in which we vary only R_{xy}). For the SCADA nudging cases (labeled S01–S03), we test values of $R_{xy} = 2, 4$, and 10 km. For the WHi lidar nudging cases (labeled L01–L14 and LC04), we assimilate upwind observations at a height of 104.5 m. The tested values of the radius of influence are $R_{xy} = 10$, 20, 30, 40, 50, and 60 km. We remind the reader that the WHi lidar is situated 47 km further from the wind farm sites and that the key aspect is to leverage these upwind observations. In addition, for the lidar FDDA cases with a radius of influence R_{xy} of 20 km (as in, e.g., Cheng et al., 2017) and 30 km, we consider five values of nudging strength G_q: $6 \times 10^{-4} \, \mathrm{s^{-1}}$ (a default value, e.g., in Cheng et al., 2017), values of $3 \times 10^{-3}, 6 \times 10^{-3}, 9 \times 10^{-3} \, \mathrm{s^{-1}}$, and the strongest value of $3 \times 10^{-2} \, \mathrm{s^{-1}}$. This yields 10 numerical experiments. Furthermore, for the nudging strength of $6 \times 10^{-3} \, \mathrm{s^{-1}}$, we consider four additional cases with a radius of influence of 10, 40, 50, and 60 km.

Finally, we propose a practical routine for hour-ahead predictions in which FDDA of upwind lidar data is performed in a consecutive manner. In this routine (labeled "LC04" in Table 3 and in subsequent figures), upwind lidar data are assimilated for 1 h, and their effect propagates as the simulation runs. Once this 1 h window elapses, the DA ends, and the model continues to run without further assimilation. This leads to prediction improvements solely due to the downwind propagation of advanced wind information induced by the FDDA effect. Given the distance of approximately 47 km from the Westhinder lidar to the Belgian–Dutch cluster, this implies an advection time of 20–70 min and a lasting effect of the DA after its end. This procedure can be repeated as many times as desired, using WRF restart files to ensure the model has spun up. Every restart should be considered a separate forecast simulation initiated at the time of the completion of lidar data collection (ideally available in real time), so in this view, no future data are assimilated in the model. Improvements can be achieved in any area of interest, provided the data source is upwind. In this configuration, this is the case when the wind is from the southwest.

3 Results and discussion

This section is dedicated to comparing the results from the simulations at the five locations of interest (the upwind Belgian WHi lidar; the front WTs and waked WTs at the selected Belgian wind farm; and finally, the two Dutch lidars,

Table 3. All simulations performed within the F2 time frame, with the varied nudging strength G_q and the horizontal radius of influence R_{xy}. S01–03 denote three numerical experiments in which SCADA is assimilated, whereas L01–L14 are simulations with only upwind lidar assimilation. In all of these simulations, the assimilation time window over which each observation point is used in the nudging algorithm is $\tau = 0.6667\,\mathrm{h}$ (40 min). Finally, LC04 is the lidar consecutive assimilation configuration for hour-ahead predictions, in which $\tau = 0.16667\,\mathrm{h}$ (10 min).

	$G_q = 6 \times 10^{-4}\,\mathrm{s}^{-1}$	$G_q = 3 \times 10^{-3}\,\mathrm{s}^{-1}$	$G_q = 6 \times 10^{-3}\,\mathrm{s}^{-1}$	$G_q = 9 \times 10^{-3}\,\mathrm{s}^{-1}$	$G_q = 3 \times 10^{-2}\,\mathrm{s}^{-1}$
$R_{xy} = 2\,\mathrm{km}$			S01		
$R_{xy} = 4\,\mathrm{km}$			S02		
$R_{xy} = 10\,\mathrm{km}$			S03		
$R_{xy} = 10\,\mathrm{km}$			L01		
$R_{xy} = 20\,\mathrm{km}$	L02	L03	L04, LC04	L05	L06
$R_{xy} = 30\,\mathrm{km}$	L07	L08	L09	L10	L11
$R_{xy} = 40\,\mathrm{km}$			L12		
$R_{xy} = 50\,\mathrm{km}$			L13		
$R_{xy} = 60\,\mathrm{km}$			L14		

EPL and LEG). In Sect. 3.1, we discuss the results from the sensitivity study on nudging parameters in F2, and we identify optimal FDDA configurations. These configurations are then applied to F1, F3, and F4 in Sect. 3.2.

3.1 Results from the numerical experiments in F2 on FDDA practices

The focus is on the day-long case of 17 February 2022 (F2 in Table 2), with the goal to study the sensitivity effects of varying the radius of influence R_{xy} and the nudging strength G_q of FDDA while nudging either lidar or SCADA data every 10 min. As previously mentioned, Table 3 summarizes all 18 cases of numerical experiments within F2: nudging SCADA with a different radius of influence and nudging lidar with different parameters. We remind the reader that for the FDDA of a lidar measurement point at 104.5 m, six values for the radius of influence R_{xy} were tested (10, 20, 30, 40, 50, and 60 km), whereas for SCADA FDDA, 2, 4, and 10 km were considered. FDDA of solely upwind observations (in this case, from the Westhinder lidar) allows for advanced wind information to propagate to the wind farms in the Belgian–Dutch cluster for (an order of) 20–70 min in advance.

The effect of a different radius of influence and nudging strength can be seen in Fig. 4. This figure shows the difference with and without FDDA of upwind lidar for three different cases:

- L02 (Fig. 4a) with $R_{xy} = 20\,\mathrm{km}$ and with the default (and lowest) nudging strength value $G_q = 6 \times 10^{-4}\,\mathrm{s}^{-1}$,

- L04 (Fig. 4b) with $R_{xy} = 20\,\mathrm{km}$ and with a 10 times larger nudging strength $G_q = 6 \times 10^{-3}\,\mathrm{s}^{-1}$,

- L14 (Fig. 4c) with $R_{xy} = 60\,\mathrm{km}$ and $G_q = 6 \times 10^{-3}\,\mathrm{s}^{-1}$.

Figure 4 shows the importance of the two nudging parameters R_{xy} and G_q. Varying their values results in wind field modifications. Figure 4 further illustrates both positive and negative variations in wind speed values within the difference fields on the left, likely attributed to numerical diffusion and advection in the proximity of the nudged region.

To explore the performance of the numerical experiments in F2, we compute the MAEs for each measurement height with respect to the WHi lidar profile, at the WHi lidar location of assimilation (for verification purposes). This is the averaged profile in time frame F2. In Fig. 5, we visualize these MAEs for all different simulations (listed on the x axis) in which lidar data are assimilated (see Table 3), as well as the two baseline simulations: a simulation with WFP only (a control run with no FDDA) and a simulation without any WFP. It is indeed expected that MAEs are always reduced at the assimilation location WHi when lidar FDDA is performed there. Although the assimilated lidar data point is positioned at a measurement height of 104.5 m, we observe enhancements in the entire profile, evident in both wind speed (Fig. 5a) and wind direction (Fig. 5b). This widespread improvement in height is attributed to the default setting of the vertical radius of influence in FDDA, which spans all model levels. Hence, the absence of vertical constraints in this influence helps avoid the formation of unusual profiles. Consequently, the assimilation of a lidar data point at a single height leads to improvements observed throughout the entire profile. In terms of horizontal influence, improvements are especially pronounced when the horizontal radius of influence R_{xy} and the nudging strength G_q are set to higher values (as seen for example in L06 and L11). However, when the default value is used for G_q (as in L02 and L07), the reduction in MAEs is not as substantial. It is also worth noting the improvements in the routine in which nudging occurs at consecutive intervals, namely case F2 WFP FDDA LC04.

For a full evaluation and determination of optimal FDDA practices, we analyze all experiments within F2, detailed in Table 3, by presenting wind speed RMSEs and biases
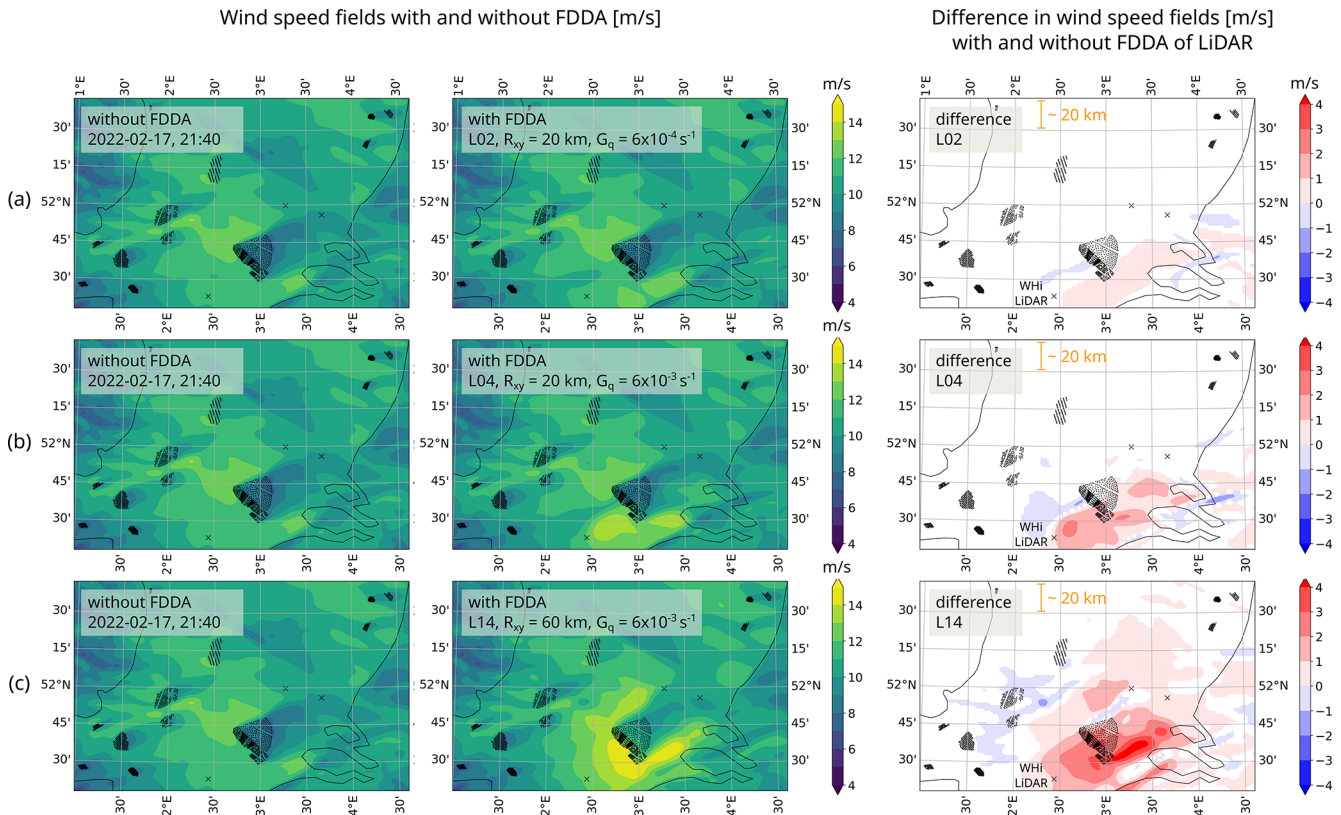
Figure 4. Snapshots of wind speed fields ($\mathrm{m\,s^{-1}}$) on 17 February at 21:40 UTC of simulations L02 **(a)**, L04 **(b)**, and L14 **(c)**. In the left columns, the results are without assimilation, whereas in the middle columns FDDA is active. Finally, in the right columns, the differences between the two are shown, along with a reference distance length of 20 km.

in Fig. 6 at different locations. Additional error data on wind direction and power are shown in Appendix B. Figure 6 illustrates the numerical results at five locations, benchmarked against local observations. For enhanced clarity, the cells which coincide with an assimilation location have been crossed out, directing attention to improvements at more distant locations. It is particularly encouraging that the FDDA of the WHi lidar point (at a height of 104.5 m) leads to improvements in results 47 km downwind at turbine sites, outperforming the baseline simulations without FDDA (F2 WFP_off and F2 WFP). When utilizing the default nudging strength value of $6 \times 10^{-4}\,\mathrm{s^{-1}}$, relatively small error reductions are observed downwind at the turbine locations (front and waked WTs) in L02 and L07, with L07 outperforming L02 due to its greater horizontal radius of influence (30 km). Similarly, among other pairs with equal nudging strength but differing horizontal radii of influence, L08 surpasses L03, L10 outperforms L05, and L11 excels over L06 due to the greater radius value. The cases L01, L04, L09, L12, L13, and L14 share a nudging strength of $6 \times 10^{-3}\,\mathrm{s^{-1}}$, with horizontal radii of influence spanning 10 km for L01 to 60 km for L14. Interestingly, L09 that has $R_{xy} = 30$ km demonstrates the most substantial error reduction in this group: increasing the radius beyond 40 km leads

to increased biases, as shown in Fig. 6b. Thus, L04 and L09 (with horizontal radii of 20 and 30 km, respectively) become apparent balanced configurations. Furthermore, while examining varied nudging strengths with a fixed radius R_{xy} of 20 km (L02, L03, L04, L05, L06) and 30 km (L07, L08, L09, L10, L11), we find consistent RMSE and bias improvements as nudging strength is increased while $R_{xy} = 20$ km. Yet, at 30 km biases worsen despite (inconsistent) RMSE gains. Thus, $R_{xy} = 20$ km is identified as an optimal choice for a horizontal radius of influence. Among L04, L05, and L06, no significant differences are present, which leads to the selection of L04 as the preferred FDDA setting. Therefore, the parameters of L04 and/or L06 are applied in Sect. 3.2 for F1, F3, and F4, as well as in a proposed consecutive assimilation routine for F2 in the current section. Finally, in Fig. 6, at the more distant EPL and LEG lidar comparison locations (approximately 110 km away from the assimilation at WHi lidar), wind speed fields remain largely unaffected. At EPL and LEG, a small influence is captured only when the horizontal radius of influence reaches 50 or 60 km.

Figure 7 shows results in the waked WT location for three variables: wind speed, wind direction, and power. The wind speed values are again normalized by a cutoff speed (31 $\mathrm{m\,s^{-1}}$). The power is also normalized by a typical rated
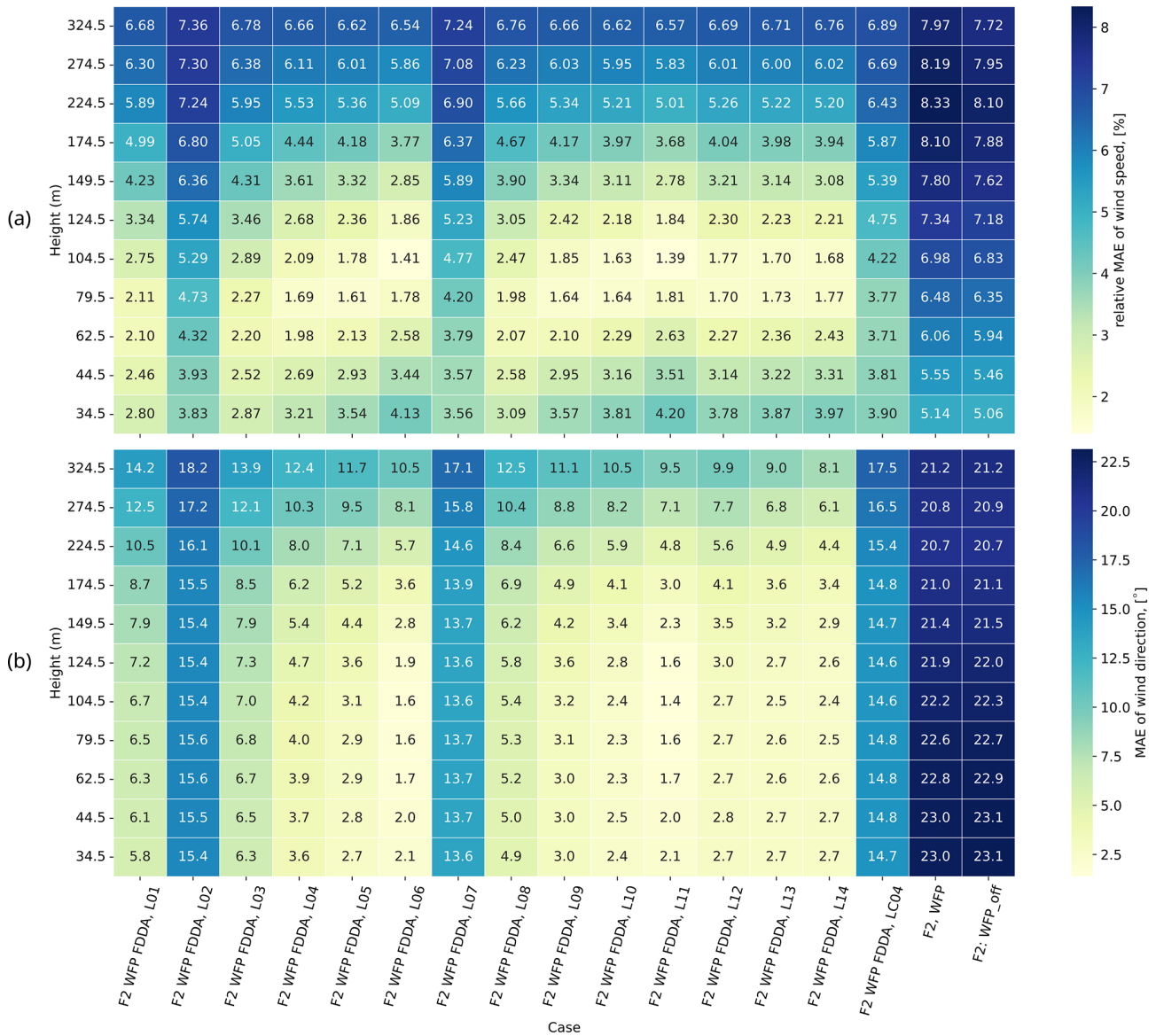
Figure 5. MAEs at the WHi assimilation location, computed for each measurement height with respect to the mean profiles from the Westhinder lidar observations for simulations in F2.

value (8.4 MW). These results are obtained when nudging only WHi lidar upwind. The comparison to SCADA data is at farm sites that are 47 km downwind. When performing FDDA of lidar, improvements in results downwind (at the waked WTs) are evident based on the reduced MAEs in the legends of Fig. 7 for (a) wind speed, (b) wind direction, and (c) power. Although the WHi lidar is located 47 km away from the wind farm of interest, the wind direction is favorable and from mostly southwest and allows the nudged information to propagate towards the zone of interest (at the Belgian wind farms).

Having upwind observations proves to be especially useful based on the results so far. Overall, the use of nudging shows a significant improvement compared to simulations

without it. This methodology can be used as long as local observations are available, but in order to utilize this in a forecasting setting, it is required to understand the behavior of the FDDA method when the data stop being fed into the simulation. Therefore, to expose the reach of this method, we explore a numerical experiment of FDDA for hour-ahead predictions in which nudging occurs at consecutive intervals that consist of a data assimilation window followed by a forecasting window. Ideally, real-time data access would be a requirement. We nudge the simulation variables closer to observations, similarly to in the previous sections, but only during short (1 h) periods of time (nudging windows, abbreviated as "NWs"). Note that these nudging windows are different from the assimilation time window τ, which defines
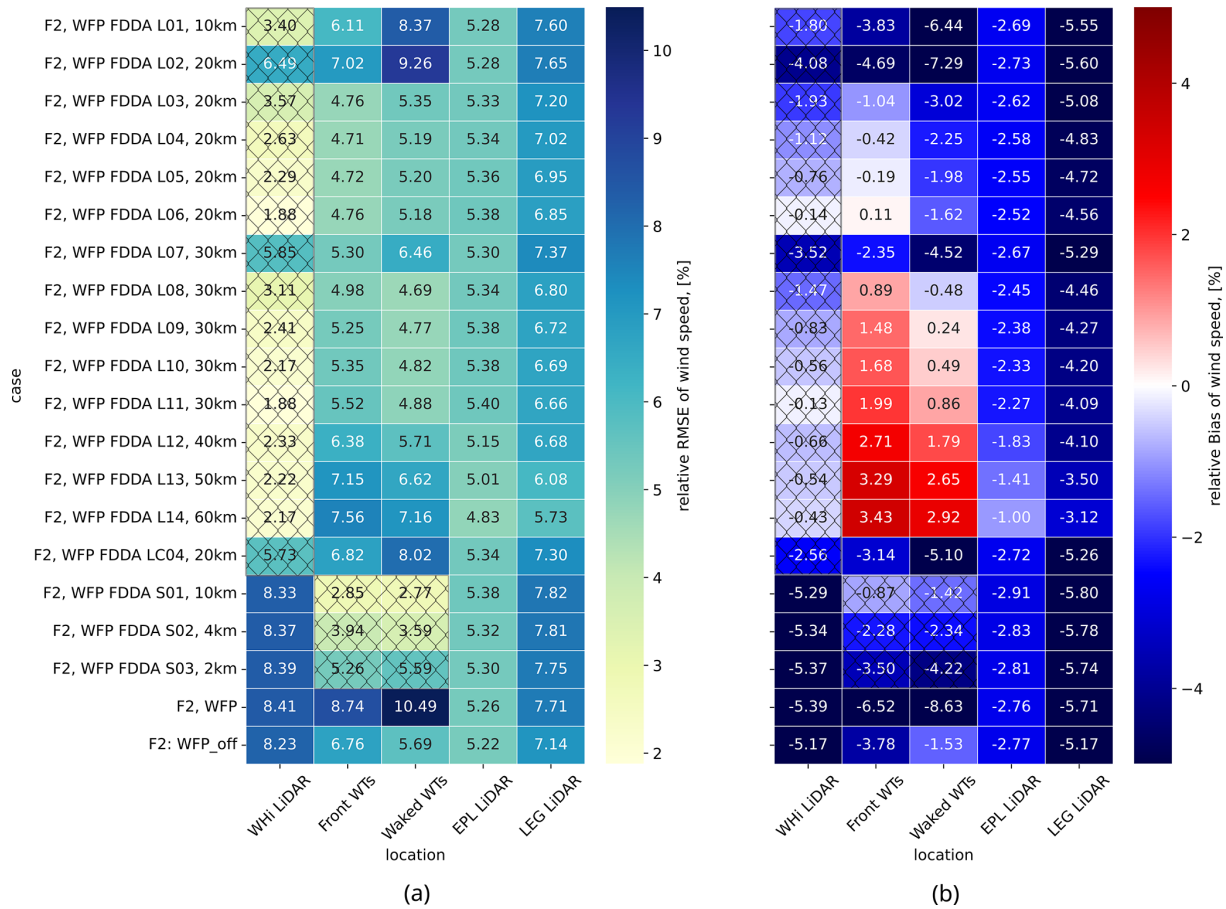
Figure 6. Color maps of MAE (**a**) and bias (**b**) for wind speed for the different simulations computed at the five locations with respect to the corresponding observations: WHi at 104.5 m, EPL at 116 m, LEG at 115 m, and front and waked WTs at hub height. Results at assimilation locations are marked with crossed-out cells.

the amount of time for which a single observation is considered in the nudging algorithm (τ is responsible for the temporal weighing function w_t in W_q of the algorithm). The assimilation is done again at the WHi lidar upwind with a nudging radius of influence of 20 km and with a nudging strength of L04. Figure 8a shows the wind speed simulation results for F2 (17 February 2022) at the WHi lidar while assimilating wind data at a height of 104.5 m in four nudging windows, each with a duration of 1 h. The first nudging window (NW1) is from 12:00 to 13:00 UTC, followed by a forecasting window (FCW1) of 2 h; the second nudging window (NW2) is from 15:00 to 16:00 UTC, followed by another forecasting window (FCW2), and so on. Each new nudging window begins with a restart of the simulation. As expected, at the nudging location, wind speed gets closer to the lidar observations within the nudging time. However, we also observe in Fig. 8b that those quantities still follow the SCADA observations downwind more closely, even after the end of the nudging window (in the first hour of all forecasting windows). This is explained by the prominently positioned lidar observations with respect to the wind farm from the Belgian–

Dutch cluster. This position allows for the assimilated quantities (during the nudging window) to be propagated downwind to the wind farm. This advection time is of the order of 1 h, and therefore the wind variables at the wind farm are still influenced after the assimilation has stopped. These lead to improved model output downwind at the waked wind turbines, as indicated for example by the reduced MAE values in Fig. 8b for normalized wind speed: from 0.09 to 0.06.

We thus demonstrated a routine with four consecutive nudging and forecasting windows to showcase the potential for hour-ahead improved predictions. A lidar that is strategically situated (such as in all of these case studies) can become an essential asset for wind farm decision-making, especially for extreme weather events like a storm or a frontal passage. Due to the enormous impact that these events might have on wind farm operators, it can be expected that the use of this method will motivate more measurement campaigns offshore, with real-time data access. The main limitation of this strategy is when the flow direction is not from southwest, as we would no longer have lidar observations upstream with respect to this direction; in that case, the wind farm is no
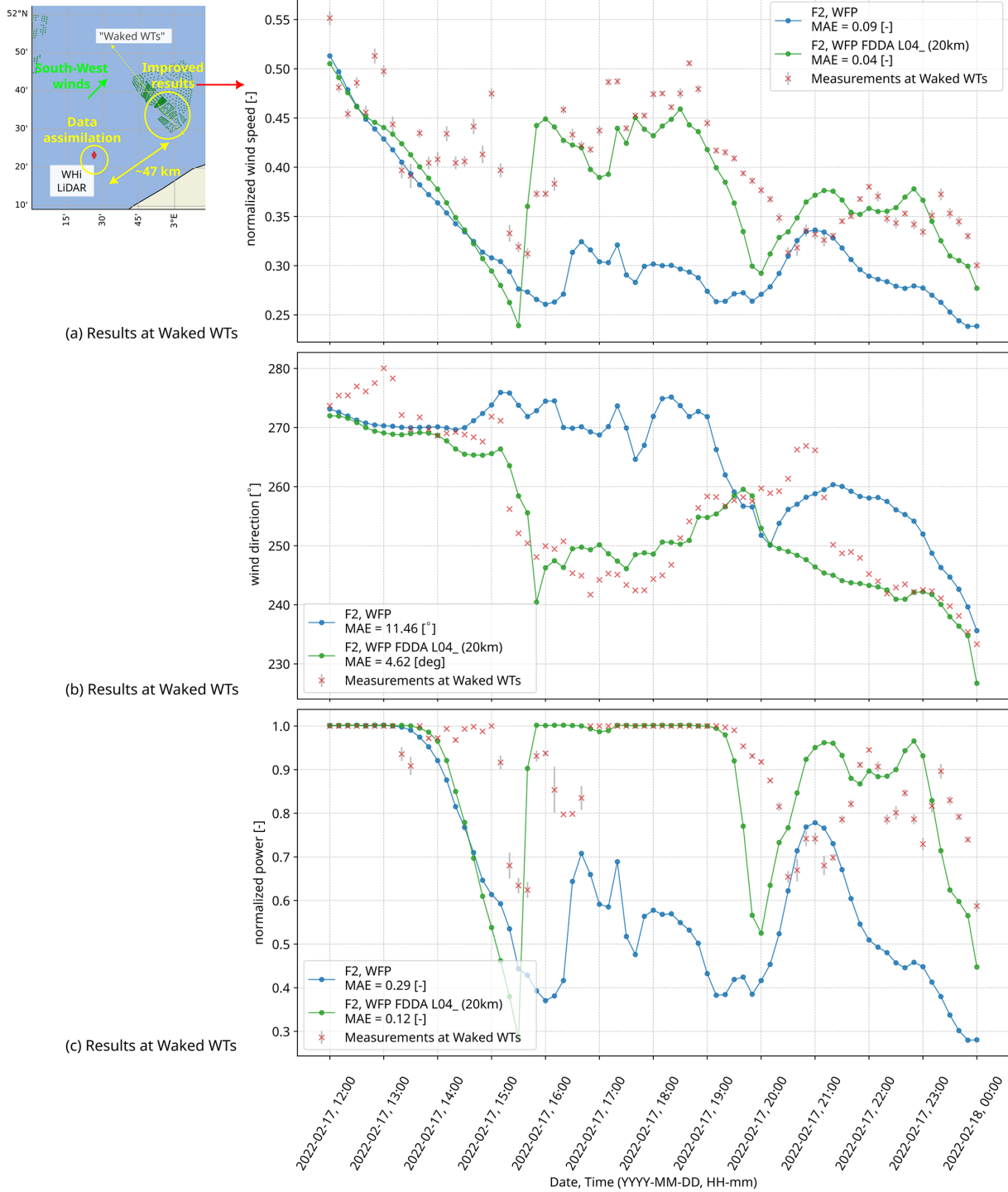
Figure 7. Simulation results with and without assimilating upwind WHi lidar (F2 WFP FDDA L04) that are compared to SCADA data from waked WTs. Wind speed **(a)**, wind direction **(b)**, and power **(c)**. Improvements when performing FDDA are highlighted by displaying the MAE values for each variable in the legends. The gray error bars indicate the standard error (available from SCADA only for wind speed and power).
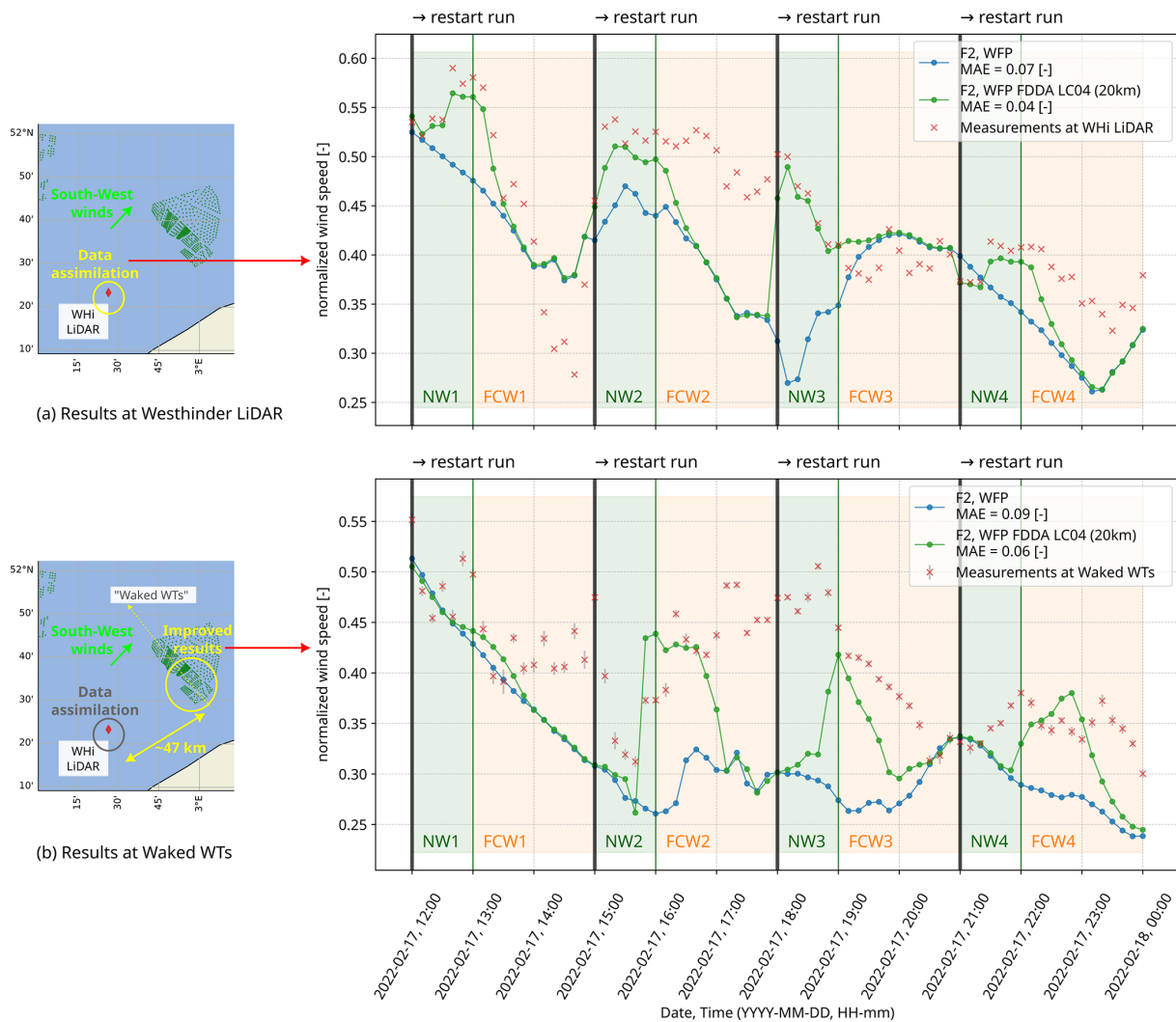
Figure 8. Artificial consecutive routine, F2 WFP FDDA LC04, for hour-ahead predictions: wind speed results at the Westhinder platform **(a)** compared to the assimilated lidar data at a height of 104.5 m in four nudging windows (denoted as NW1–4, 1 h each). Information is propagated downwind to the location of the waked WTs, and the results are compared to SCADA **(b)**. Forecasting windows have a 2 h length and are denoted as FCW1–4. The gray error bars indicate the standard error (available from SCADA only for wind speed and power).

longer downwind of the nudged quantity and therefore remains (almost) unaffected.

3.2 Results for cases with different weather conditions using WFP and FDDA

We discuss results obtained for time frames from Table 2 (F1, F3, and F4) using the findings from the sensitivity study on nudging parameters in Sect. 3.1. Let us first illustrate results with and without the presence of wind turbines in the computational domain in Fig. 9 for F1. This figure displays snapshots of wind fields for three arbitrary time slots during this period of interest in February 2022. The wind directions for the three snapshots in Fig. 9 are from the southwest (a), south (b), and west (c). Significant velocity deficits are ob-

served in all cases, as well as inter-farm interactions. For the whole duration of the 4 d long time frame F1, simulation results at the waked WT location are shown in Fig. 10. These results are for both the F1 WFP case (with active WFP) and the F1 WFP FDDA L04 case (with active WFP and with FDDA of lidar located further upwind). The wind speed values are normalized by a representative cut-out speed (31 m s^{-1}). We remind the reader that the details on nudging values for L04 are in Table 3. The results using WFP captures the storms in F1 and swift wind direction changes well, especially before and during Storm Franklin (19 February 2022 at 18:00 UTC, 20 February 2022 at 21:00 UTC). In order to further enhance the model output during the three extreme events, we perform FDDA of upwind WHi lidar data every 10 min for the whole duration of F1, which sig-
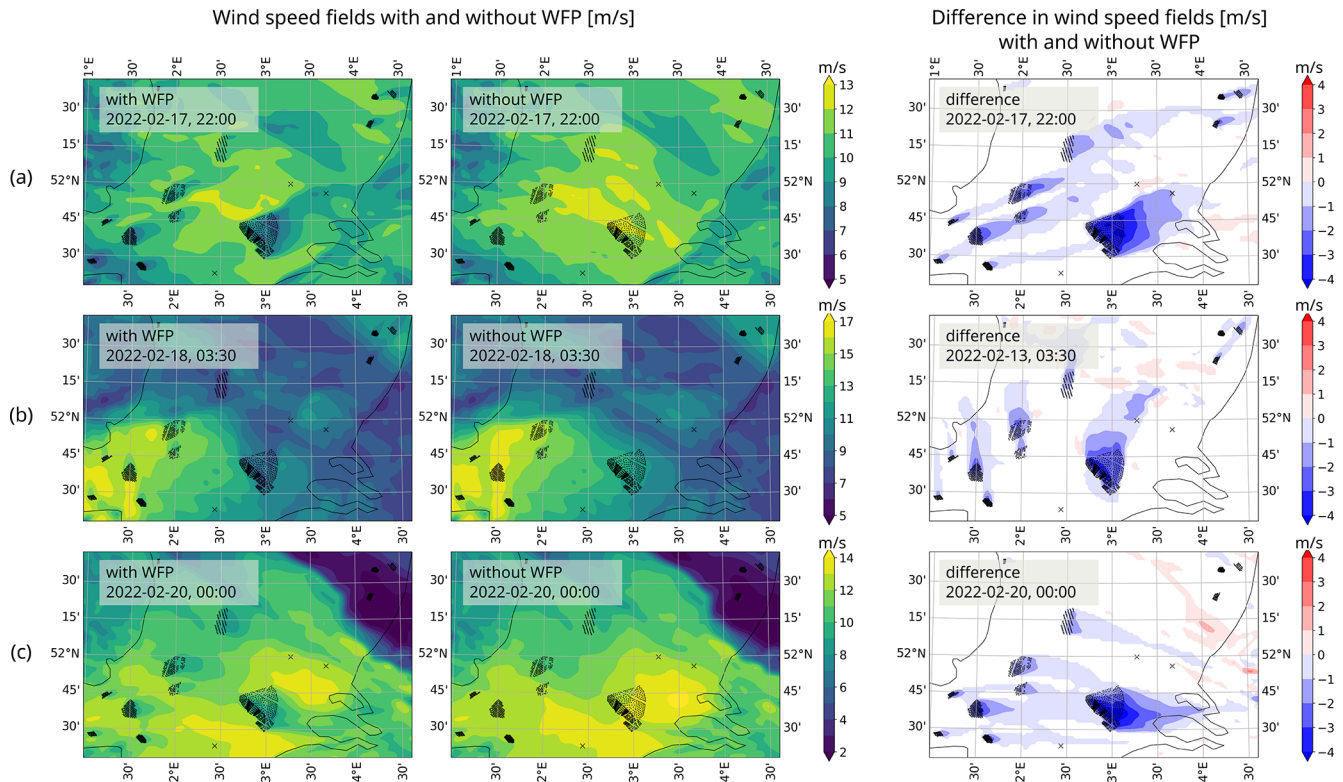
Figure 9. Snapshots of wind speed fields (m s^{-1}) for three different time instances within F1 **(a–c)**. In the left column, results with active WFP show that energy is indeed extracted from the flow. The middle fields are from the simulation without WFP. On the right, the difference in wind speed fields with and without WFP is shown.

nificantly improves the results of wind speed and wind directions, as indicated by the reduced MAE values for the F1 WFP FDDA (L04) case in Fig. 10.

To evaluate the performance of the different scenarios in wind speed and wind direction results, we present their errors, summarized in Fig. 11. This involves time frames F1, F3, and F4, with their corresponding options (without WFP, with WFP, and with FDDA) at the waked WT location. The FDDA configuration used is also specified (L04 or L06 from Table 3, the choice of which is supported by the sensitivity study in Sect. 3.1). Moreover, Fig. 11a emphasizes that activating WFP helps improve wind speed but not wind direction. This is the case for F1 and F4, except if the relative bias of wind speed with respect to SCADA data is already negative when WFP is inactive. In that case, the wind power extraction will further increase this bias to more negative values, as is the case for F3 in Fig. 11c. Therefore, for frame F3, activating WFP does not improve the MAE of wind speed, as shown in Fig. 11a. Activating WFP has almost no impact on wind direction MAEs (Fig. 11b) and biases (Fig. 11d). However, the introduction of the upwind lidar FDDA improves both wind speed and wind direction. FDDA of such observations provides enhanced results that are useful for weather reanalysis and detailed wind resource assessment.

4 Conclusions

This study demonstrated the usefulness of assimilating local offshore observations (such as lidar) in NWP models (in this case, via the FDDA algorithm in the Advanced Research WRF model) to improve simulation results of wind speed; wind direction; and, consequently, power production, based on error reduction during four selected case studies. The simulation results included wind farms in the domain. One of the case studies involved two extreme weather events in February 2022, which were captured well by the simulations. Moreover, we explored the leverage of the FDDA method in a day-long frame by assimilating data either from an upwind (WHi) lidar at a specific height or solely from SCADA at hub height. We performed a sensitivity study via 18 numerical experiments that have eight different values for a radius of influence of DA and five different values for nudging strength. This helped to identify an optimal FDDA configuration for this offshore setting. We highlighted the benefits of having an upwind lidar, since its assimilation improves results 47 km downwind at the location of the wind farm. To benefit from this configuration, the only requirement is to have the most common wind direction (which for the Southern Bight of the North Sea is from the southwest). The experiments of upwind lidar FDDA exhibited improve-
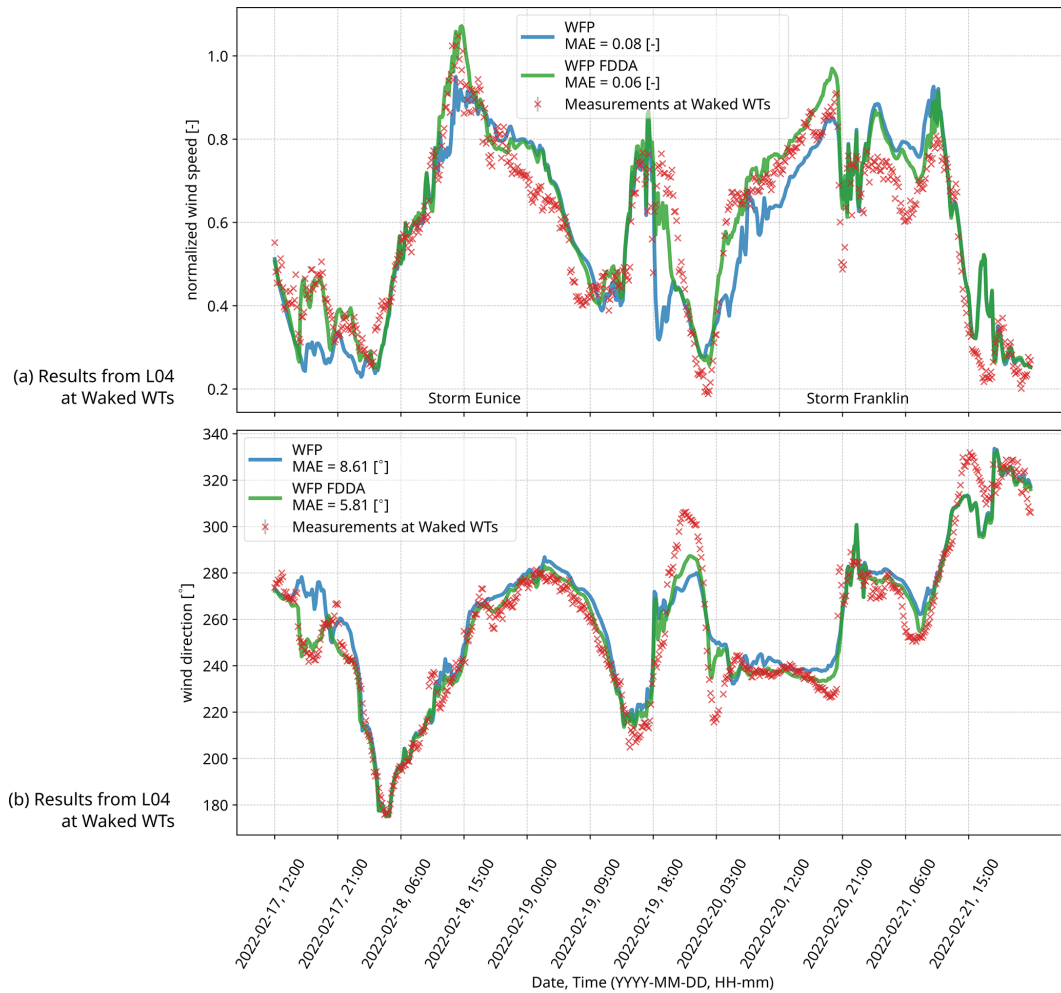
Figure 10. The simulations F1 WFP and F1 WFP FDDA (L04) when assimilating (upwind) lidar data 47 km away: results at the waked WT location during storms Eunice and Franklin (in UTC).

ments in results, which were quantified by MAEs, RMSEs, and bias, with respect to the local observations. The identified optimal FDDA setting was also applied to three more case studies. Furthermore, after demonstrating the leverage of upwind nudging, we explored a forecasting routine that contains consecutive nudging windows, which also showed improvements in hour-ahead predictions that were quantified via MAEs.

Limitations of this work include the requirement for a specific range of values for wind direction: the assimilation of Westhinder lidar data would not have shown improvements in the downstream region of interest if the wind direction was not from the southwest. Additionally, the lack of offshore observations (especially in real time) due to the harsh offshore conditions that impact measurement campaigns (as well as the cost of deployment and maintenance and structural limitations in deeper waters) reduces the geographical areas in which this method can be applied. Another important limitation is that only prognostic variables can be as-

similated with the FDDA method, which is why variational methods are widely used and hold potential for future works. It is worth mentioning that the nudging of waked turbines can affect the physical evolution of turbine and farm wakes at typical mesoscale resolutions that do not resolve individual turbine wakes. A detailed study on this is left for future work. Furthermore, with the increasing density of wind farms installed in the North Sea, the assimilation of SCADA data from neighboring wind farms in NWP models is an important topic for future research.

The methods in this work can be valuable in the future for long-term refined reanalysis (several weeks to a few years), where the assimilation of offshore data acquired during the wind farm pre-development phase can help reduce bias errors and/or reduce the risk of under-sampling extremes or where the goal is to evaluate the effects of wind farm decommission on present farms. Practical implications for the wind energy industry can be derived from this research: by utilizing open-source NWP models such as WRF, which is
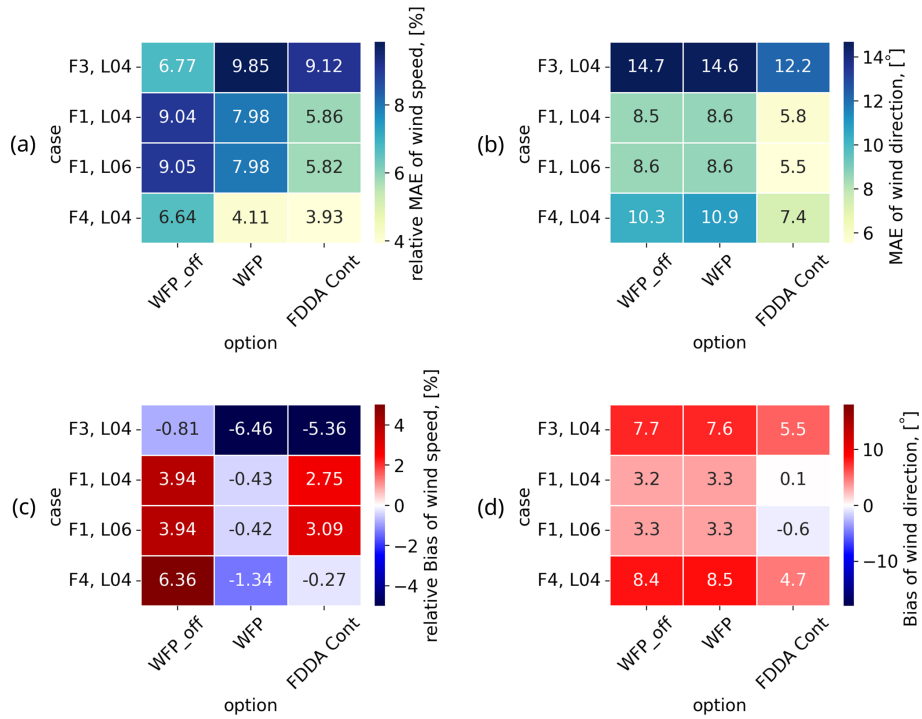
Figure 11. Mean absolute errors (MAEs) of wind speed **(a)** and wind direction **(b)**, computed for each case at the waked WT location. Bias of wind speed **(c)** and wind direction **(d)** for each case at the waked WT location. Data are assimilated only at WHi lidar (47 km away).

designed for both atmospheric research and operational forecasting applications, more informed wind farm planning and decision-making strategies can be pursued, even under extreme weather conditions. This is especially feasible if offshore measurement campaigns continue to be motivated.

Appendix A: Wind farms included in the numerical setup

The wind farms included in the numerical setup are described in Table A1, using data from Hoeser et al. (2022) and Hoeser and Kuenzer (2022).

Table A1. Details on wind farms (listed in no particular order) in the Southern Bight of the North Sea, summarized from Hoeser et al. (2022).

Wind farm name	Total number of turbines	Turbine capacity	Hub height (m)	Rotor diameter (m)
Borssele I Borssele II	94	8.4 MW	107	164
Borssele III Borssele IV	77	9.5 MW	107	164
Borssele V	2	9.5 MW	107	164
Thorntonbank I	6	5.0 MW	93.3	126
Thorntonbank II & III	48	6.15 MW	93.3	126
Rentel	42	7.35 MW	102	154
Northwind	72	3.0 MW	80.1	112
SeaMade (Seastar)	30	8.4 MW	107	164
Norther	44	8.4 MW	107	164
Nobelwind	50	3.3 MW	77.1	112
Belwind	55	3.0 MW	70.1	112
Belwind Alstom Haliade	1	6.0 MW	98.1	150
Northwester 2	23	9.5 MW	107	164
SeaMade (Mermaid)	28	8.4 MW	107	164
Scroby Sands	30	2.0 MW	68	80
East Anglia ONE	102	7 MW	120	154
Galloper	56	6 MW	88	154
Greater Gabbard	140	3.6 MW	78	107
Gunfleet Sands	48	3.6 MW	78	107
Gunfleet Sands	2	6 MW	84	120
London Array	175	3.6 MW	87	120
Kentish Flats	30	3 MW	70	90
Kentish Flats	15	3.3 MW	83.6	112
Thanet	100	3 MW	70	90
Luchterduinen	43	3 MW	81	112
Egmond aan Zee	36	3 MW	70	90
Princess Amalia	60	2 MW	60	80

figurations that have an active WFP. These improvements are quite significant, considering the (almost twice as high) error values in the F2 WFP case (when no data are assimilated). The results in both figures are consistent with the analysis in Sect. 3.1 for wind speed.

Appendix B: Supplementary color maps of errors for wind direction and power in F2

To support the findings on optimal FDDA settings based on wind speed error reduction in Sect. 3.1, we include the errors for wind direction and power. Figure B1 contains wind direction RMSEs and biases that showcase significant improvements when FDDA is performed (especially for the preferred configurations L04 and L06). Figure B2 displays power improvements for RMSE and bias for all FDDA con-
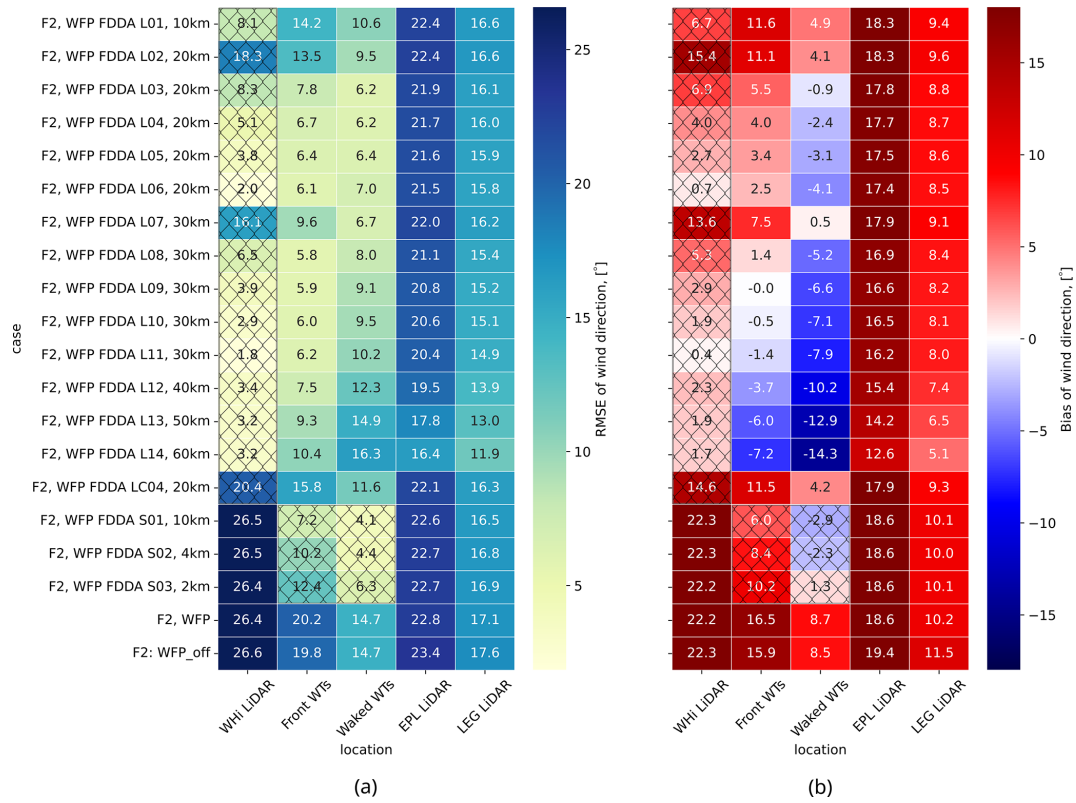
Figure B1. Color maps of MAE **(a)** and bias **(b)** for wind direction for the different simulations computed at the five locations with respect to the corresponding observations: WHi at 104.5 m, EPL at 116 m, LEG at 115 m, and front and waked WTs at hub height. Results at assimilation locations are marked with crossed-out cells.
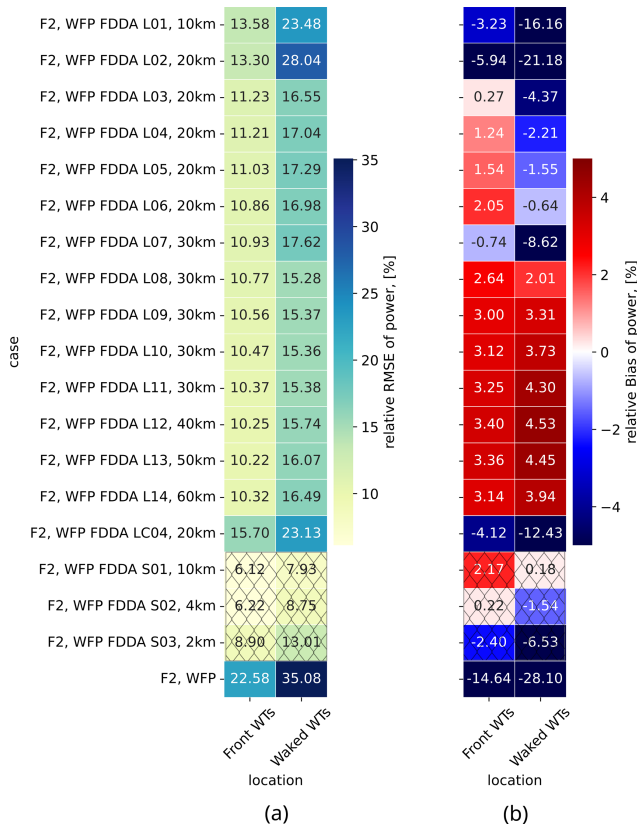
Figure B2. Color maps of MAE **(a)** and bias **(b)** for power for the different simulations (with an active WFP) computed at the two wind farm locations (front and waked WTs) at hub height. Results at assimilation locations are marked with crossed-out cells.

Disclaimer. Publisher's note: Copernicus Publications remains neutral with regard to jurisdictional claims made in the text, published maps, institutional affiliations, or any other geographical representation in this paper. While Copernicus Publications makes every effort to include appropriate place names, the final responsibility lies with the authors.

Code and data availability. The Advanced Research WRF (ARW) model was developed by the National Center for Atmospheric Research (https://doi.org/10.5065/1DFH-6P97, Skamarock et al., 2019). WRF v4.5.1 is a publicly available code at https://github.com/wrf-model/WRF/releases/tag/v4.5.1 (Community developed code, 2023). The forcing data used for initial and boundary conditions in the WRF simulations are also publicly available at the NCEP GFS 0.25 Degree Global Forecast Grids Historical Archive (https://doi.org/10.5065/D65D8PWK, National Centers for Environmental Prediction et al., 2015). Data from the numerical simulations and the namelists used in the WRF model are available upon reasonable request. The postprocessing routines were built using the wrf-python library (https://doi.org/10.5065/D6W094P1, Ladwig, 2017). The Westhinder lidar data were collected under the framework of the SeaFD project, supported by the Flanders Innovation & Entrepreneurship (VLAIO) fund at the von Karman Institute for Fluid Dynamics. The lidar datasets at the Lichteiland Goeree platform and at the Europlatform are available thanks to the TNO Measurement Program of the Wind Energy Research Group at TNO Energy Transition (https://nimbus.windopzee.net/, TNO Wind Energy Research Group, 2023). Finally, the SCADA observations of the wind farm of interest, as well as details regarding the wind turbines, are under a non-disclosure agreement (NDA).

Review statement. This paper was edited by Rebecca Barthelmie and reviewed by two anonymous referees.

References

Ali, K., Schultz, D. M., Revell, A., Stallard, T., and Ouro, P.: Assessment of Five Wind-Farm Parameterizations in the Weather Research and Forecasting Model: A Case Study of Wind Farms in the North Sea, Mon. Weather Rev., 151, 2333–2359, https://doi.org/10.1175/mwr-d-23-0006.1, 2023.

Archer, C. L., Colle, B. A., Delle Monache, L., Dvorak, M. J., Lundquist, J., Bailey, B. H., Beaucage, P., Churchfield, M. J., Fitch, A. C., Kosovic, B., Lee, S., Moriarty, P. J., Simao, H., Stevens, R. J. A. M., Veron, D., and Zack, J.: Meteorology for Coastal/Offshore Wind Energy in the United States: Recommendations and Research Needs for the Next 10 Years, B. Am. Meteorol. Soc., 95, 515–519, https://doi.org/10.1175/bams-d-13-00108.1, 2014.

Archer, C. L., Wu, S., Ma, Y., and Jiménez, P. A.: Two Corrections for Turbulent Kinetic Energy Generated by Wind Farms in the WRF Model, Mon. Weather Rev., 148, 4823–4835, https://doi.org/10.1175/mwr-d-20-0097.1, 2020.

Barker, D., Huang, X.-Y., Liu, Z., Auligné, T., Zhang, X., Rugg, S., Ajjaji, R., Bourgeois, A., Bray, J., Chen, Y., Demirtas, M., Guo, Y.-R., Henderson, T., Huang, W., Lin, H.-C., Michalakes, J., Rizvi, S., and Zhang, X.: The Weather Research and Forecasting Model's Community Variational/Ensemble Data Assimilation System: WRFDA, B. Am. Meteorol. Soc., 93, 831–843, https://doi.org/10.1175/bams-d-11-00167.1, 2012.

Barker, D. M., Huang, W., Guo, Y.-R., Bourgeois, A. J., and Xiao, Q. N.: A Three-Dimensional Variational Data Assimilation System for MM5: Implementation and Initial Results, Mon. Weather Rev., 132, 897–914, https://doi.org/10.1175/1520-0493(2004)132<0897:atvdas>2.0.co;2, 2004.

Belgian Offshore Platform News: Stormy February drives offshore energy production to new record, https://www.belgianoffshoreplatform.be/en/news/stormy-february-drives-offshore-energy-production-to-new-record/ (last access: 23 August 2023), 2022.

Cheng, W. Y., Liu, Y., Bourgeois, A. J., Wu, Y., and Haupt, S. E.: Short-term wind forecast of a data assimilation/weather forecasting system with wind turbine anemometer measurement assimilation, Renew. Energy, 107, 340–351, https://doi.org/10.1016/j.renene.2017.02.014, 2017.

Community developed code: WRF Version 4.5.1 (Bug-fix Release), GitHub [code], https://github.com/wrf-model/WRF/releases/tag/v4.5.1 (last access: 21 January 2025), 2023.

Dörenkämper, M., Olsen, B. T., Witha, B., Hahmann, A. N., Davis, N. N., Barcons, J., Ezber, Y., Garciá-Bustamante, E., González-Rouco, J. F., Navarro, J., Sastre-Marugán, M., Sile, T., Trei, W., Žagar, M., Badger, J., Gottschall, J., Rodrigo, J. S., and Mann, J.: The Making of the New European Wind Atlas – Part 2: Production and evaluation, Geosci. Model Dev., 13, 5079–5102, https://doi.org/10.5194/gmd-13-5079-2020, 2020.

Ek, M. B., Mitchell, K. E., Lin, Y., Rogers, E., Grunmann, P., Koren, V., Gayno, G., and Tarpley, J. D.: Implementation of Noah land surface model advances in the National Centers for Environmental Prediction operational mesoscale Eta model, J. Geophys. Res.-Atmos., 108, 8851, https://doi.org/10.1029/2002jd003296, 2003.

Eriksson, O., Baltscheffsky, M., Breton, S.-P., Söderberg, S., and Ivanell, S.: The Long distance wake behind Horns Rev I

studied using large eddy simulations and a wind turbine parameterization in WRF, J. Phys.: Conf. Ser., 854, 012012, https://doi.org/10.1088/1742-6596/854/1/012012, 2017.

Fischereit, J., Brown, R., Larsén, X. G., Badger, J., and Hawkes, G.: Review of Mesoscale Wind-Farm Parametrizations and Their Applications, Bound.-Lay. Meteorol., 182, 175–224, https://doi.org/10.1007/s10546-021-00652-y, 2022a.

Fischereit, J., Hansen, K. S., Larsén, X. G., van der Laan, M. P., Réthoré, P.-E., and Leon, J. P. M.: Comparing and validating intra-farm and farm-to-farm wakes across different mesoscale and high-resolution wake models, Wind Energ. Sci., 7, 1069–1091, https://doi.org/10.5194/wes-7-1069-2022, 2022b.

Fitch, A. C., Olson, J. B., Lundquist, J. K., Dudhia, J., Gupta, A. K., Michalakes, J., and Barstad, I.: Local and mesoscale impacts of wind farms as parameterized in a mesoscale NWP model, Mon. Weather Rev., 140, 3017–3038, https://doi.org/10.1175/MWR-D-11-00352.1, 2012.

Glabeke, G., Buckingham, S., De Mulder, T., and van Beeck, J.: Anomalous wind events over the Belgian North Sea at heights relevant to wind energy, Wind Energy Science Conference 2023 Mini-Symposium 1.5 IEA Wind Task 52: Replacing met masts and Accelerating offshore wind deployment, Submission Number 438, https://zenodo.org/record/8034397 (last access: 21 January 2025), 2023.

Grell, G., Dudhia, J., and Stauffer, D.: A description of the fifth-generation Penn State/NCAR Mesoscale Model (MM5), UCAR/NCAR, https://doi.org/10.5065/D60Z716B, 1994.

Hahmann, A. N., Sile, T., Witha, B., Davis, N. N., Dörenkämper, M., Ezber, Y., Garciá-Bustamante, E., González-Rouco, J. F., Navarro, J., Olsen, B. T., and Söderberg, S.: The making of the New European Wind Atlas – Part 1: Model sensitivity, Geosci. Model Dev., 13, 5053–5078, https://doi.org/10.5194/gmd-13-5053-2020, 2020.

Hoeser, T. and Kuenzer, C.: DeepOWT: A global offshore wind turbine data set, Zenodo [data set], https://doi.org/10.5281/ZENODO.5933967, 2022.

Hoeser, T., Feuerstein, S., and Kuenzer, C.: DeepOWT: a global offshore wind turbine data set derived with deep learning from Sentinel-1 data, Earth Syst. Sci. Data, 14, 4251–4270, https://doi.org/10.5194/essd-14-4251-2022, 2022.

Huang, X.-Y., Xiao, Q., Barker, D. M., Zhang, X., Michalakes, J., Huang, W., Henderson, T., Bray, J., Chen, Y., Ma, Z., Dudhia, J., Guo, Y., Zhang, X., Won, D.-J., Lin, H.-C., and Kuo, Y.-H.: Four-Dimensional Variational Data Assimilation for WRF: Formulation and Preliminary Results, Mon. Weather Rev., 137, 299–314, https://doi.org/10.1175/2008mwr2577.1, 2009.

Iacono, M. J., Delamere, J. S., Mlawer, E. J., Shephard, M. W., Clough, S. A., and Collins, W. D.: Radiative forcing by long-lived greenhouse gases: Calculations with the AER radiative transfer models, J. Geophys. Res., 113, D13103, https://doi.org/10.1029/2008jd009944, 2008.

Kain, J. S.: The Kain–Fritsch Convective Parameterization: An Update, J. Appl. Meteorol., 43, 170–181, https://doi.org/10.1175/1520-0450(2004)043<0170:tkcpau>2.0.co;2, 2004.

Kosovic, B., Haupt, S. E., Adriaansen, D., Alessandrini, S., Wiener, G., Monache, L. D., Liu, Y., Linden, S., Jensen, T., Cheng, W., Politovich, M., and Prestopnik, P.: A Comprehensive Wind Power Forecasting System Integrating Artificial Intel-

ligence and Numerical Weather Prediction, Energies, 13, 1372, https://doi.org/10.3390/en13061372, 2020.

Ladwig, B.: wrf-python (Version 1.3.4) [Software], UCAR/NCAR [code], https://doi.org/10.5065/D6W094P1, 2017.

Larsén, X. G. and Fischereit, J.: A case study of wind farm effects using two wake parameterizations in the Weather Research and Forecasting (WRF) model (V3.7.1) in the presence of low-level jets, Geosci. Model Dev., 14, 3141–3158, https://doi.org/10.5194/gmd-14-3141-2021, 2021.

Larsén, X. G., Du, J., Bolaños, R., Imberger, M., Kelly, M. C., Badger, M., and Larsen, S.: Estimation of offshore extreme wind from wind-wave coupled modeling, Wind Energy, 22, 1043–1057, https://doi.org/10.1002/we.2339, 2019.

Lee, J. C. Y. and Lundquist, J. K.: Evaluation of the wind farm parameterization in the Weather Research and Forecasting model (version 3.8.1) with meteorological and turbine power data, Geosci. Model Dev., 10, 4229–4244, https://doi.org/10.5194/gmd-10-4229-2017, 2017.

Liu, Y., Warner, T. T., Bowers, J. F., Carson, L. P., Chen, F., Clough, C. A., Davis, C. A., Egeland, C. H., Halvorson, S. F., Huck, T. W., Lachapelle, L., Malone, R. E., Rife, D. L., Sheu, R.-S., Swerdlin, S. P., and Weingarten, D. S.: The Operational Mesogamma-Scale Analysis and Forecast System of the U.S. Army Test and Evaluation Command. Part I: Overview of the Modeling System, the Forecast Products, and How the Products Are Used, J. Appl. Meteorol. Clim., 47, 1077–1092, https://doi.org/10.1175/2007jamc1653.1, 2008.

Lydia, M., Kumar, S. S., Selvakumar, A. I., and Kumar, G. E. P.: A comprehensive review on wind turbine power curve modeling techniques, Renew. Sustain. Energ. Rev., 30, 452–460, https://doi.org/10.1016/j.rser.2013.10.030, 2014.

Mylonas, M., Barbouchi, S., Herrmann, H., and Nastos, P.: Sensitivity analysis of observational nudging methodology to reduce error in wind resource assessment (WRA) in the North Sea, Renew. Energy, 120, 446–456, https://doi.org/10.1016/j.renene.2017.12.088, 2018.

Nakanishi, M. and Niino, H.: An Improved Mellor–Yamada Level-3 Model: Its Numerical Stability and Application to a Regional Prediction of Advection Fog, Bound.-Lay. Meteorol., 119, 397–407, https://doi.org/10.1007/s10546-005-9030-8, 2006.

National Centers for Environmental Prediction, National Weather Service, NOAA, and US Department of Commerce: NCEP GFS 0.25 Degree Global Forecast Grids Historical Archive, Research Data Archive at the National Center for Atmospheric Research, Computational and Information Systems Laboratory [data set], https://doi.org/10.5065/D65D8PWK, 2015.

Peña, A., Mirocha, J. D., and van der Laan, M. P.: Evaluation of the Fitch Wind-Farm Wake Parameterization with Large-Eddy Simulations of Wakes Using the Weather Research and Forecasting Model, Mon. Weather Rev., 150, 3051–3064, https://doi.org/10.1175/mwr-d-22-0118.1, 2022.

Porchetta, S., Muñoz-Esparza, D., Munters, W., van Beeck, J., and van Lipzig, N.: Impact of ocean waves on offshore wind farm power production, Renew. Energy, 180, 1179–1193, https://doi.org/10.1016/j.renene.2021.08.111, 2021.

Pryor, S. C. and Barthelmie, R. J.: A global assessment of extreme wind speeds for wind energy applications, Nat. Energy, 6, 268–276, https://doi.org/10.1038/s41560-020-00773-7, 2021.

Reen, B.: A brief guide to observation nudging in WRF, https://raw.githubusercontent.com/wrf-model/obsgrid/master/obsnudgingguide.pdf (last access: 21 January 2025), 2016.

Reen, B. P. and Stauffer, D. R.: Data Assimilation Strategies in the Planetary Boundary Layer, Bound.-Lay. Meteorol., 137, 237–269, https://doi.org/10.1007/s10546-010-9528-6, 2010.

Sethunadh, J., Letson, F. W., Barthelmie, R. J., and Pryor, S. C.: Assessing the impact of global warming on windstorms in the northeastern United States using the pseudo-global-warming method, Nat. Hazards, 117, 2807–2834, https://doi.org/10.1007/s11069-023-05968-1, 2023.

Skamarock, W. C. and Klemp, J. B.: A time-split nonhydrostatic atmospheric model for weather research and forecasting applications, J. Comput. Phys., 227, 3465–3485, https://doi.org/10.1016/j.jcp.2007.01.037, 2008.

Skamarock, W. C., Klemp, J. B., Dudhia, J., Gill, D. O., Liu, Z., Berner, J., Wang, W., Powers, J. G., Duda, M. G., Barker, D. M., and Huang, X.-Y.: A Description of the Advanced Research WRF Model Version 4.3, NSF [code], https://doi.org/10.5065/1DFH-6P97, 2019.

Sun, W., Liu, Z., Song, G., Zhao, Y., Guo, S., Shen, F., and Sun, X.: Improving Wind Speed Forecasts at Wind Turbine Locations over Northern China through Assimilating Nacelle Winds with WRFDA, Weather Forecast., 37, 545–562, https://doi.org/10.1175/WAF-D-21-0041.1, 2022.

Thompson, G., Field, P. R., Rasmussen, R. M., and Hall, W. D.: Explicit Forecasts of Winter Precipitation Using an Improved Bulk Microphysics Scheme. Part II: Implementation of a New Snow Parameterization, Mon. Weather Rev., 136, 5095–5115, https://doi.org/10.1175/2008mwr2387.1, 2008.

TNO Wind Energy Research Group: TNO Measurement Program, TNO Energy Transition, LiDAR measurements at Lichteiland Goeree (LEG) and at Europlatform (EPL), https://nimbus.windopzee.net/ (last access: 21 January 2025), 2023.

Vemuri, A., Buckingham, S., Munters, W., Helsen, J., and van Beeck, J.: Sensitivity analysis of mesoscale simulations to physics parameterizations over the Belgian North Sea using Weather Research and Forecasting – Advanced Research WRF (WRF-ARW), Wind Energ. Sci., 7, 1869–1888, https://doi.org/10.5194/wes-7-1869-2022, 2022.

Wang, Y., Hu, Q., Li, L., Foley, A. M., and Srinivasan, D.: Approaches to wind power curve modeling: A review and discussion, Renew. Sustain. Energ. Rev., 116, 109422, https://doi.org/10.1016/j.rser.2019.109422, 2019.

Xu, M., Liu, Y., Davis, C. A., and Warner, T. T.: Sensitivity study on nudging parameters for a mesoscale FDDA system, in: vol. 19, AMS, Conference on weather analysis and forecasting, 13 August 2002, Texas, 127–130, https://ams.confex.com/ams/SLS_WAF_NWP/techprogram/paper_47401.htm (last access: 21 January 2025), 2002.

Yang, B., Zhong, L., Wang, J., Shu, H., Zhang, X., Yu, T., and Sun, L.: State-of-the-art one-stop handbook on wind forecasting technologies: An overview of classifications, methodologies, and analysis, J. Clean. Product., 283, 124628, https://doi.org/10.1016/j.jclepro.2020.124628, 2021.

ZephIR: ZephIR Lidar 2018 WALTZ – a user's guide, version 2.2, https://s.campbellsci.com/documents/au/product-brochures/zephir_premium.pdf (last access: 21 January 2025), 2018.

Zhang, X., Huang, X.-Y., and Pan, N.: Development of the Up-graded Tangent Linear and Adjoint of the Weather Research and Forecasting WRF) Model, J. Atmos. Ocean. Tech., 30, 1180–1188, https://doi.org/10.1175/jtech-d-12-00213.1, 2013.

Zhang, X., Huang, X.-Y., Liu, J., Poterjoy, J., Weng, Y., Zhang, F., and Wang, H.: Development of an Efficient Regional Four-Dimensional Variational Data Assimilation System for WRF, J. Atmos. Ocean. Tech., 31, 2777–2794, https://doi.org/10.1175/jtech-d-13-00076.1, 2014.

Zhao, X., Wang, S., and Li, T.: Review of Evaluation Criteria and Main Methods of Wind Power Forecasting, Energ. Proced., 12, 761–769, https://doi.org/10.1016/j.egypro.2011.10.102, 2011.